DESIGN, MODELING AND SIMULATION OF PLANAR WAVEGUIDE TIME DOMAIN OPTICAL FOURIER TRANSFORMER

DESIGN, MODELING AND SIMULATION OF PLANAR WAVEGUIDE TIME DOMAIN OPTICAL FOURIER TRANSFORMER

By

Rui Tang, B.Sc.

A Thesis

Submitted to the School of Graduate Studies

in Partial Fulfilment of the Requirements

for the Degree

Master of Applied Science

McMaster University

MASTER OF APPLIED SCIENCE (2011) McMaster University

(Electrical and Computer Engineering) Hamilton, Ontario

TITLE:	Design, Modeling and Simulation of Planar Waveguide Time Domain Optical Fourier Transformer
AUTHOR:	Rui Tang
	B.Sc. (Wuhan University, China)
SUPERVISOR:	Dr. Xun Li
	Professor, Department of Electrical and Computer Engineering
NUMBER OF PAGES:	xi, 75

Abstract

With the development of ultrafast pulse technology, Time Domain Optical Fourier Transformer (TD-OFT) has been a popular research topic. It can be used in various applications such as ultrafast optical communication, spectro-temporal imaging, time-resolved spectroscopy and optical signal processing. By utilizing planar waveguide lenses and diffraction gratings, a novel TD-OFT is proposed in this thesis. Compared with the currently developed TD-OFT made by the discrete photonic and optoelectronic component, this device can offer the intrinsic advantage of integration and seems more appealing on the simulated performance and fabrication cost.

The scalar diffraction theory, including Fourier transform properties of lens and the pupil function of the blazed phase grating, is first presented. It is the basic theory for the design of TD-OFT.

Later, a detailed theoretical model of TD-OFT is developed by mathematical derivation. In order to verify the results, the reciprocity in TD-OFT is also explored. The simulations based on analytical results are investigated to show how the device performance, demonstrated by the similarity coefficient, may be affected by the structural parameters or the input pulses. It is found that similarity increases as the device aperture increases. For the input pulse, under the circumstance of same similarity, the shorter temporal pulse duration with larger bandwidth needs smaller aperture size.

Finally, a more accurate numerical simulation carried by the Extension of Beam propagation method (EX-BPM) is performed to verify the design concept. Two specific examples, Gaussian and raised cosine input signals with same pulse duration 10 fs, are chosen to study the device performance. The results show that by utilizing the TD-OFT with a designed size about 600 μm (in width)$\times$5 mm (in length), the similarity between the output temporal profile and the Fourier transform profile of the original pulse can be achieved above 97%. To make the device size even smaller, we can either reduce the focal length of the collimating lens or enlarge the bandwidth of input pulse.

Acknowledgements

I would like to express my deepest gratitude to my supervisor Dr. Xun Li. This thesis would not have been possible without his remarkable help and inspiration. Not only does he give excellent guidance, generous support and constant encouragement in my academic study, but he also offers invaluable advices and perspectives which are of substantial benefit to my whole life.

I greatly appreciate Dr. Wei-Ping Huang and Dr. Mohamed Bakr for their expert teaching and enlightening discussions throughout the important course of my M.Sc program. I also would like to acknowledge my teaching assistant supervisor, Dr. Shiva Kumar and Dr. Tim Davidson, for their numerous help in my work.

I am very grateful to my colleagues, Dr. Guirong Zhou, Dr. Yanping Xi, Dr. Jianwei Mu, Xiaojun Liang, Kan He, Qingyi Guo, Lanxin Deng, Yu Li and Han Lin for their useful discussions in research and various assistances in daily life. I would like to thank Ms. Cheryl Gies, Ms. Helen Jachna and Mr. Terry Greelay for their administrative and technical support.

Last but not least, I would like to give special thanks from the bottom of my heart to my dearest family. It is their deepest love and lifelong care that encourage me to move forward.

Contents

List of Figures

List of Tables

Chapter 1
Introduction

1.1 Background of the Research

Over the past two decades, revolutionary breakthroughs have occurred in the field of ultrafast pulse technology. The most common generation source is mode-locked laser, which offers femtosecond pulse duration with substantially increased average power. Recently, diode pumped mode-locked Yb3+ laser with pulse as short as 71 fs and an average power of 1.09 W has been reported [1]. To obtain even shorter pulses, other approaches based for example on high order harmonics generation of short optical pulses in rare gases are being actively investigated. Recent progress have been made even in the attosecond regime [2] .

Within this context, Time Domain Optical Fourier Transformer (TD-OFT) is of significant interest in the ultrafast pulse field. It offers various potential applications including but not limited to ultrafast real time measurements [3], pulse compression [4], spectro-temporal imaging [5], time-resolved spectroscopy [6], ultrafast optical signal processing [7] and realization of OFDM system [8].

A complete TD-OFT causes the temporal and spectral envelopes of a signal to swap such that the temporal profile is converted to the spectrum domain while spectrum profile is transferred to the time domain. Such transformations are in close analogy with

traditional spatial domain Fourier transforms by a spatial lens, therefore, the TD-OFD can be viewed as a "time lens."

1.2 Reviews of the Conventional TD-OFT

T. Jannson theoretically proposed the implementation of time lens based on space–time duality of electromagnetic waves in 1983[9]. The duality indicates that the pulse spreading in time as it propagates in a dispersive medium is equivalent with the paraxial diffraction of beams in space. In that sense, the quadratic time-varying phase shift across the temporal envelop of the pulse is imparted to a wide input pulse, which is entirely equivalent to the action of a thin spatial lens [10, 11]. Several approaches have been proposed to perform this imparting.

The first demonstration of time lens is utilizing self-phase modulation in an optical fiber, with subsequent compression in a dispersive delay line such as diffraction grating pair [12]. Cross-phase modulation between the original input signal and an intense pump pulse in a nonlinear fiber can lead to impart a quadratic phase to the input wave [13]. As a result, the output spectrum is the image of the initial temporal profile. However, since chirping by self-phase modulation is a nonlinear optical process which is intensity dependent, high input optical power is required in order to add large phase shifts. Besides, the quadratic temporal shape of the pump pulse can be maintained only within a portion of the pulse duration.

Another optical time lens utilized electro-optic (EO) phase modulator was demonstrated by Kolner and Nazarathy in 1989 [14]. An optical wave was imparted a

locally quadratic phase profile when it propagated under the cusp of a sinusoidal drive field in the EO crystal, thereby allowing the modulator to act as a time lens as show in Figure 1.1. Different from the self-phase modulation which relies on the interaction between the pulse and a passive medium, this approach depends on the driving power and frequency [15]. However, in this method, the time window has to be narrowed down due to the fact that an ideal quadratic phase modulation and low aberrations are obtained only within a region of about one-sixth of a modulation period. In addition, since the driving voltage is restricted to the maximum voltage tolerable by the modulator, the range of phase shift that can be imparted to the input signal is therefore greatly limited [16].

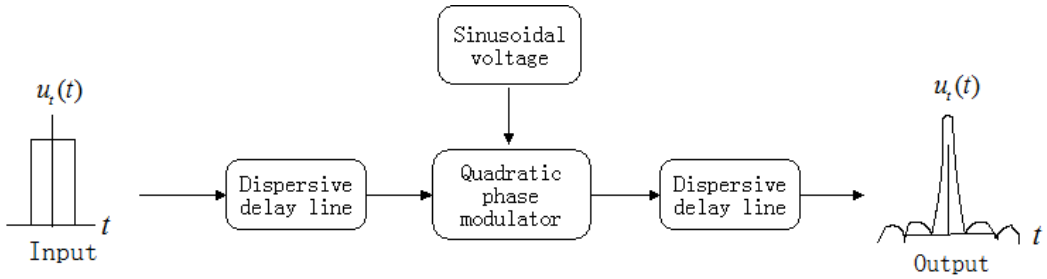

Figure 1.1 TD-OFT configuration utilized EO phase modulator.

It has been proven that the space-time duality is also applicable to the reflection of pulse from linearly chirped fiber gratings (LCFG) [17]. For this purpose, J. Azaña and M. A. Muriel have developed the design of OFT based on linearly chirped fiber gratings (LCFG) instead of conventional quadratic phase modulation as shown in Figure 1.2. In this scheme, the LCFG can be particularly designed to yield the desired dispersion characteristics, which makes the system work as a Fourier Transformer.

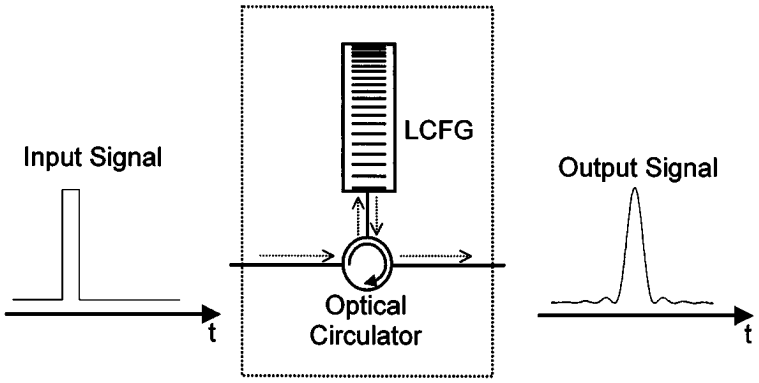

Figure 1.2 TD-OFT configuration utilized LCFG.

Optical parametric wave-mixing process can also been applied to realize time lens [16, 18]. Such as the sum-frequency or difference-frequency generation with chirped pump pulses. And more recently, Cornell University has proposed a time lens based on four-wave mixing (FWM) in a silicon nanowaveguide. Figure 1.3 is the temporal telescopic system consisting of two FWM time lenses. The time lens can produces more than 100π of phase shift to the input signal , which is not readily achievable using other approaches such as electro-optic phase modulators [19]. Nevertheless, the amplitude noise present on the input pulse will be increased by parametric wave-mixing process.

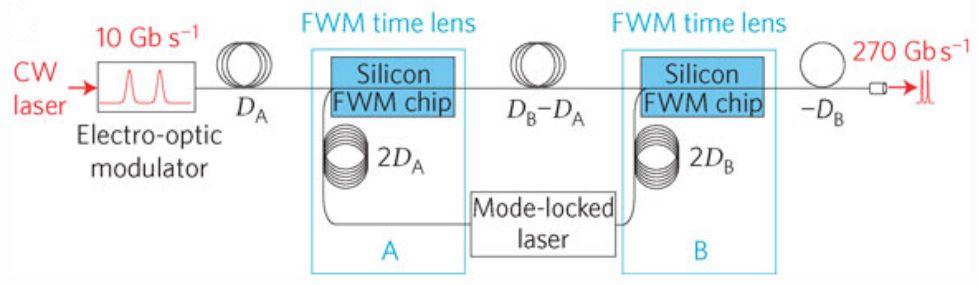

Figure 1.3 Temporal telescopic system based on FWM time lens.

1.3 Motivation of the Research

TD-OFT can be demonstrated by discrete photonic and optoelectronic components as presented above. However, a critical bottleneck in such setups is the

difficulty in integration, thus hampering widespread implementation. On one hand, the discrete setups suffer easily from misalignment due to mechanical and thermal influence [20]. On the other hand, the large bandwidths carried by the ultrafast pulses cannot be readily full utilized by standard electro-optical means because of the limits in digital-to-analog converter technology and high timing jitter. Therefore, a solution to the implementation of the TD-OFT in an integrated and compact optical system is highly demanded. Aiming at this goal, this thesis is devoted to exploring a novel optical integrated TD-OFT.

The TD-OFT based on planar waveguide circuit is capable of integration with a more compact size. It not only meets the high environmental stability requirements but also allows miniaturization of optical systems. Moreover, integration of planar waveguide TD-OFT on a single chip leads to relatively cost reduction. As a result, the planar waveguide TD-OFT has the significant potential in the next ultrafast optical network.

1.4 Outline of the Thesis

This thesis contains five chapters as shown in Figure 1.4. They are organized as follows .

Chapter 1 starts with the introduction to the background of ultrafast technology. A brief review of various setups for TD-OFT is then presented. Finally, the motivation of this thesis is outlined aimed at addressing the challenges in the existing TD-OFT devices.

In Chapter 2, the Fresnel and Fraunhofer diffraction are firstly presented. Then under the paraxial approximation, the mathematic description on diffraction of lens is

further derived. After that, we investigate the pupil function of the blazed phase gratings which will be used in the following chapter.

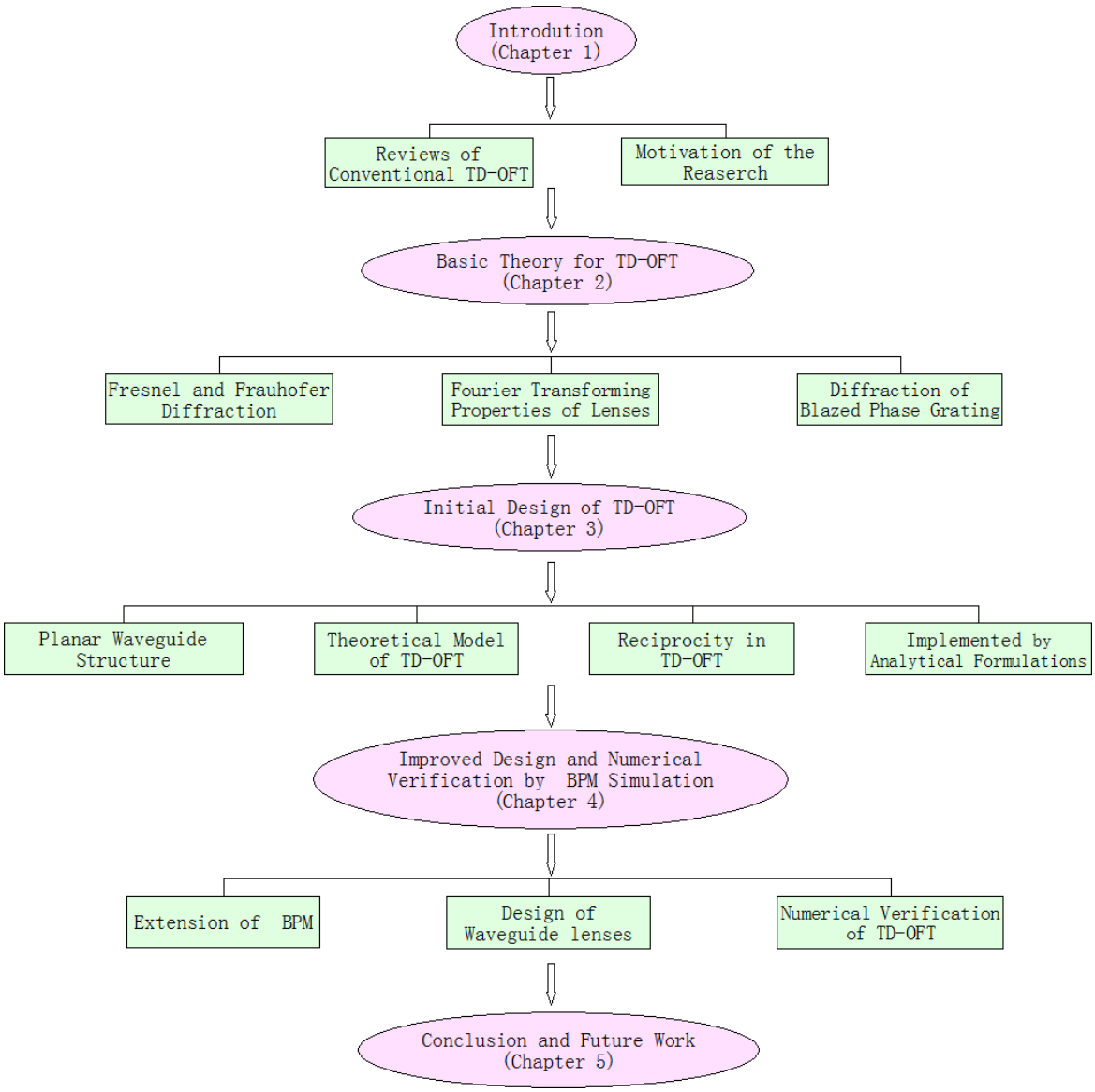

Figure 1.4 Block diagram of the outline of the thesis.

Chapter 3 focuses on the initial design of planar TD-OFT. It provides a brief description of the planar waveguide structure. Then a detailed theoretic model of

TD-OFT is proposed. In order to verify the derivation, the reciprocity in TD-OFT is also explored. Analysis of the analytical results is further investigated with several examples.

Chapter 4 gives the simulation results of the whole device. The numerical tool named as Extension of BPM (EX-BPM) is described at the beginning. Then, an improved design of waveguide lens is discussed. Next, the performance of the design is evaluated with several examples.

Chapter 5 summarizes the conclusions in this thesis and lists suggestions for future work.

1.5 Contributions of the Thesis

The major contributions of this thesis are summarized as follows:

1. The theoretical model for TD-OFT, which is composed of waveguide lenses and blazed phase gratings, is proposed. A detailed mathematical derivation based on scalar diffraction optics is presented. In order to verify the theoretical analysis, the reciprocity in TD-OFT is also studied.

2. Three different pulse examples, including the Gaussian pulse, square pulse and square pulse train, are implemented by analytical formulations.

3. Improved waveguide lens is particularly designed and then the whole device is simulated by EX-BPM with two specific pulses, Gaussian and raised cosine pulse. The simulation results are also verified by reciprocity theorem using the numerical method.

Chapter 2

Basic Theory for TD-OFT

2.1 Introduction

In optics, classical electrodynamics and quantum electrodynamics are two different approaches to describe light. Since the device in our work is used for its macroscopic properties rather than sub-microscopic ones, it deals entirely with the classical methods .When the wavelength of an electromagnetic wave is very small, approaching zero, the waves propagate in terms of rays which travel in straight lines. This can be described by geometric optics. However, the geometric optics is inadequate to depict the observed phenomena in many situations such as diffraction. Diffraction occurs when the wave meet obstacles and bend around the edges of objects. This is also the foundation of our design concept.

In this chapter, we start with the Fresnel and Fraunhofer diffraction[21]. Then the mathematic derivations on the diffraction of lens are provided based on scalar wave propagation and paraxial approximation. Moreover, the pupil function of the blazed phase gratings is investigated.

2.2 Fresnel and Fraunhofer Diffraction

When light propagates from the source plane to the observation plane as shown in

the Figure 2-1. In this figure, Z denotes the propagation direction, X can be viewed as "free space" direction, while Y indicates the confined direction where the wave is confined by a slab waveguide.

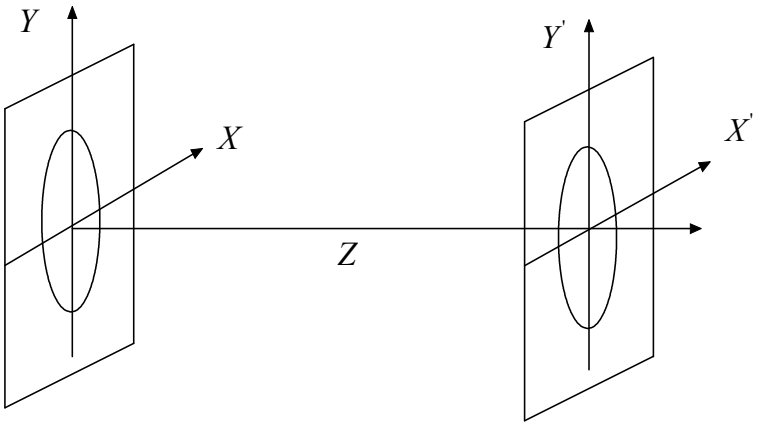

Figure 2.1 Coordinate systems for optical-wave propagation.

The scalar wave equation is given in the form of [22, 23]

$$\nabla^2 E(x,y,z) + k^2 n^2(y) E(x,y,z) = 0, \tag{2.1}$$

where $\nabla^2 = \partial^2 / x^2 + \partial^2 / y^2 + \partial^2 / z^2$, $k = 2\pi / \lambda$ is the wave propagation constant with λ as the free-space wavelength of the wave. With slab waveguide structure along Y, the filed can be decomposed as

$$E(x,y,z) = \sum_m \psi_m(y) U(x,z). \tag{2.2}$$

Substituting (2.2) into (2.1) yields

$$(\frac{\partial^2}{\partial x^2} + \frac{\partial^2}{\partial z^2}) U(x,z) \sum_m \psi_m(y) + U(x,z) \sum_m \frac{\partial^2}{\partial y^2} \psi_m(y) + U(x,z) \sum_m k^2 n^2(y) \psi_m(y) = 0. \tag{2.3}$$

Considering $\psi(y)$ is the slab waveguide mode, we must have

$$\frac{\partial^2}{\partial y^2}\psi_m(y)+k^2n^2(y)\psi_m(y)=k^2n_{eff,m}^2\psi_m(y), \tag{2.4}$$

where $n_{eff,m}$ is the effective index of the m th slab mode. Therefore, (2.3) becomes

$$\sum_m\left[\left(\frac{\partial^2}{\partial x^2}+\frac{\partial^2}{\partial z^2}\right)U(x,z)+k^2n_{eff,m}^2(y)U(x,z)\right]\psi_m(y)=0. \tag{2.5}$$

Multiplying the mode itself on both side of (2.5) and integrating over the mode spreading area

$$\sum_m\left[\left(\frac{\partial^2}{\partial x^2}+\frac{\partial^2}{\partial z^2}\right)U(x,z)+k^2n_{eff,m}^2(y)U(x,z)\right]\int_{-\infty}^{+\infty}\psi_m(y)\psi_n(y)=0. \tag{2.6}$$

According to the mode orthogonal property, we obtain the equation as follows

$$\left(\frac{\partial^2}{\partial x^2}+\frac{\partial^2}{\partial z^2}\right)U(x,z)+k^2n_{eff,m}^2(y)U(x,z)=0. \tag{2.7}$$

Assuming single guide mode is confined in the waveguide, let $n_{eff,m}=n$. $U(x,z)$ can be expanded into spatial plane waves though Fourier Transform

$$U(x,z)=\int_{-\infty}^{+\infty}\tilde{U}(f_x,z)e^{2\pi f_x x}df_x, \tag{2.8}$$

where f_x is the spatial frequency. Substituting (2.8) into (2.7), we obtain

$$\frac{\partial}{\partial^2}\tilde{U}(f_x,z)+\left[k^2n^2-\left(2\pi f_x\right)^2\right]\tilde{U}(f_x,z)=0. \tag{2.9}$$

The solution of Equation (2.9) can be solved as

$$\tilde{U}(f_x,z)=\tilde{U}(f_x,z_0)e^{jkn\sqrt{1-(\lambda f_x/n)^2}(z-z_0)}. \tag{2.10}$$

It shows that the 2D free-space behaves like a phaser. The transfer function $e^{jkn\sqrt{1-(\lambda f_x/n)^2}(z-z_0)}$ is given in the 2D form of Huygens-Sommerfeld spherical wave function. Following (2.8) and (2.10), it leads to the form of the field distribution as

$$\begin{aligned} U(x,z) &= \int_{-\infty}^{+\infty} \tilde{U}(f_x,z_0) e^{jkn\sqrt{1-(\lambda f_x/n)^2}(z-z_0)} e^{2\pi f_x x} df_x \\ &= \int_{-\infty}^{+\infty}\int_{-\infty}^{+\infty} U(x_0,z_0) e^{jkn\left[\sqrt{1-(\lambda f_x/n)^2}(z-z_0)+(\lambda f_x/n)(x-x_0)\right]} df_x dx_0, \end{aligned} \tag{2.11}$$

where $\tilde{U}(f_x,z) = \int_{-\infty}^{+\infty} U(x_0,z_0) e^{-2\pi f_x x} dx_0$ is used. By introducing the impulse response of spherical wave function, we define

$$h(x-x_0,z-z_0) = \int_{-\infty}^{+\infty} e^{jkn\left[\sqrt{1-(\lambda f_x/n)^2}(z-z_0)+(\lambda f_x/n)(x-x_0)\right]} dx_0. \tag{2.12}$$

Therefore, the propagating field can be rewritten as

$$U(x,z) = \int_{-\infty}^{+\infty} U(x_0,z_0) h(x-x_0,z-z_0) dx_0. \tag{2.13}$$

Under the paraxial approximation, (2.12) becomes

$$\begin{aligned} h(x-x_0,z-z_0) &\approx \int_{-\infty}^{+\infty} e^{jkn\{[1-\frac{1}{2}(\lambda f_x/n)^2](z-z_0)+(\lambda f_x/n)(x-x_0)\}} dx_0 \\ &= \sqrt{\frac{\pi n}{j\pi(z-z_0)}} e^{jkn[(z-z_0)+\frac{(x-x_0)^2}{2(z-z_0)}]}. \end{aligned} \tag{2.14}$$

Equation (2.13) can then be further simplified and the Fresnel (near-field) diffraction formula is obtained

$$U(x,z) = \sqrt{\frac{n}{j\lambda(z-z_0)}} e^{jkn\left[(z-z_0)+\frac{x^2}{2(z-z_0)}\right]} \int_{-\infty}^{+\infty} e^{jkn\frac{x_0^2}{2(z-z_0)}} U(x_0,z_0) e^{-jkn\frac{x}{z-z_0}x_0} dx_0. \tag{2.15}$$

When $x_0 \ll \sqrt{\lambda(z-z_0)/\pi n}$ is valid, it leads to the Fraunhofer (far-field) diffraction formula which is denoted as

$$U(x,z) \approx \sqrt{\frac{n}{j\lambda(z-z_0)}}\, e^{jkn\left[(z-z_0)+\frac{x^2}{2(z-z_0)}\right]} \int_{-\infty}^{+\infty} U(x_0,z_0) e^{-jkn\frac{x}{z-z_0}x_0}\, dx_0. \qquad (2.16)$$

From (2.16), it can be found that when light propagates very far form its source field, the optical field $U(x,z)$ turns out to be the space Fourier transformation of the source field $U(x_0,z_0)$. Besides, there is an extra factor which counts in the amplitude decay and phase delay in Z plus defocusing in X direction.

2.3 Fourier Transforming Properties of Lenses

2.3.1 Fourier Transformation Through Lens

According to the analysis in the former section, optical system design will become straightforward if the spatial Fourier transformation rule is applicable between the radiant place z_0 and the irradiant lines z. Unfortunately, equation (2.16) is only valid under the far-field assumption, which means that the spatial Fourier transformation relation only exists in lengthy optical systems with large propagation distance. However, in practical applications, we always miniaturize the systems due to the less cost and better integration. Therefore, we have to make the Fourier transformation valid even in the near-field region. For this purpose, the lens is introduced. It can impart a phase delay which cancels out the extra phase shift in Fresnel diffraction leading to its equivalence to Fraunhofer diffraction.

As a result, the space Fourier transformation is also utilizable even in the near-field area through a proper designed lens.

As an example of a simple case, assuming the lens consists of two symmetric circle arcs, whose radiuses are the same value R.The refractive indices inside and outside the lens are indicated by n_H and n_L respectively. In order to calculate the phase delay generated by lens, the thickness function should be obtained. Considering half of the lens as shown in Figure 2.2, the thickness can be denoted as

$$L_1(x) = L_1(0) - [R - \sqrt{R^2 - x^2}], \tag{2.17}$$

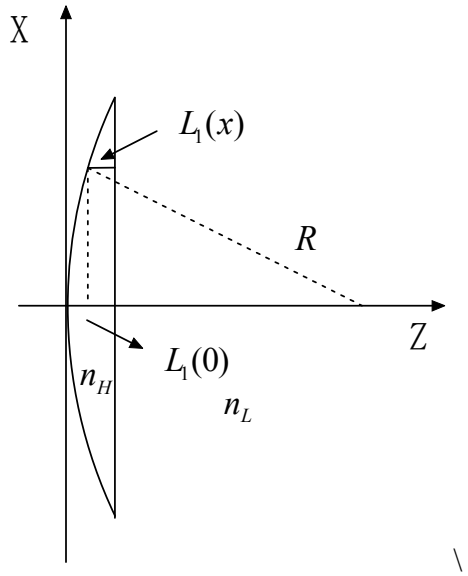

Figure 2.2 Geometry of a half thin lens.

where $L_1(0)$ is maximum thickness at the central coordinate. If $x \ll R$, (2.17) is approximated by

$$L_1(x) = L_1(0) - R[1 - \sqrt{1 - (x/R)^2}] \approx L_1(0) - x^2/(2R). \tag{2.18}$$

Therefore, the total thickness at the coordinate (x) is calculated as

$$L(x) \approx 2[L_1(0) - x^2/(2R)] = L(0) - x^2/R, \tag{2.19}$$

where $L(0) = 2L_1(0)$ is determined by R and the distance between the center of the two arcs. Referring to Figure 2.3, the total phase delay of the lens can be expressed as

$$\phi(x) = \exp(jkn_H L(0)) \exp(-jk(n_H - n_L)x^2/R). \tag{2.20}$$

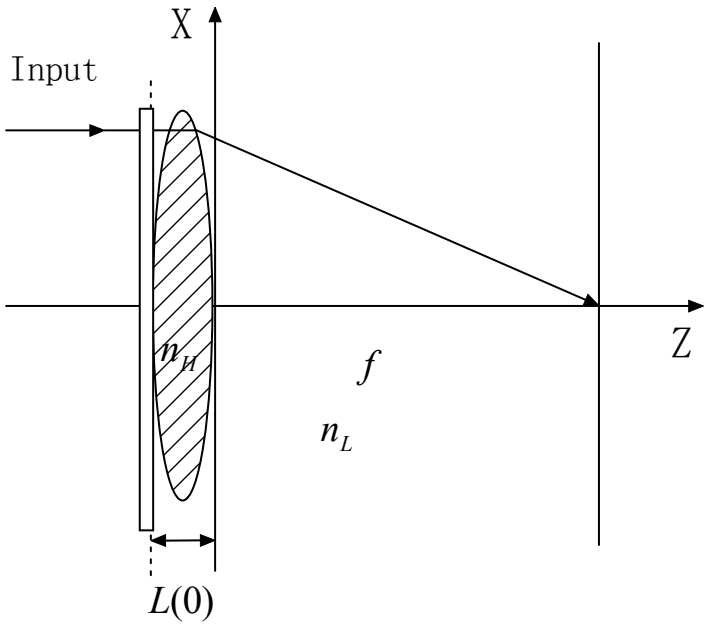

Figure 2.3 Input plane is placed directly against the lens.

In Figure 2.3, assuming that the field distribution at $z = -L(0)$ is $U(x, -L(0))$ and the aperture of the lens is large enough to be ignored. After traveling through the lens, the field at $z = 0$ is written as

$$\begin{aligned} U(x,0) &= U(x,-L(0)) \exp(j\phi(x)) \\ &= U(x,-L(0)) \exp(jkn_H L(0)) \exp(-jk(n_H - n_L)x^2/R). \end{aligned} \tag{2.21}$$

Using the Fresnel diffraction equation (2.15), we obtain

$$
\begin{aligned}
U(x,z) &= \sqrt{\frac{n}{j\lambda z}}\, e^{jkn\left[z+\frac{x^2}{2z}\right]} \int_{-\infty}^{+\infty} e^{jkn\frac{x_0^2}{2z}} U(x_0,0) e^{-jkn\frac{x}{z}x_0}\, dx_0 \\
&= \sqrt{\frac{n}{j\lambda z}}\, e^{jkn_L\left[z+\frac{x^2}{2z}\right]} e^{jkn_H L(0)} \int_{-\infty}^{+\infty} e^{jk\left[\frac{n_L}{2z}-\frac{n_H-n_L}{R}\right]x_0^2} U(x_0,-L(0)) e^{-jkn_L\frac{x}{z}x_0}\, dx_0 .
\end{aligned}
\tag{2.22}
$$

If $z = \dfrac{n_L}{2(n_H - n_L)} R = f$, equation (2.22) will change into a Fourier transform, where f is defined to be the focal length of the lens.

$$
\begin{aligned}
U(x,f) &= \sqrt{\frac{n}{j\lambda f}}\, e^{jkn_L\left[f+\frac{x^2}{2f}\right]} e^{jkn_H L(0)} \int_{-\infty}^{+\infty} U(x_0,-L(0)) e^{-j2\pi\frac{n_L}{\lambda f}xx_0}\, dx_0 \\
&= \sqrt{\frac{n}{j\lambda f}}\, e^{jkn_L\left[f+\frac{x^2}{2f}\right]} e^{jkn_H L(0)} F\{U(x_0,-L(0))\}_{f_x=\frac{n_L x}{\lambda f}} .
\end{aligned}
\tag{2.23}
$$

2.3.2 Object Before the Lens

When the source plane is placed a distance d_0 before the lens, as shown in Figure 2.4, the impulse response of Fresnel diffraction can be written as:

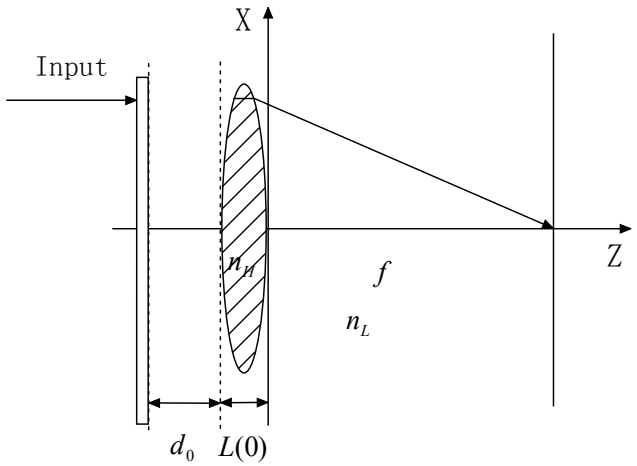

Figure 2.4 Input plane is placed a distance d_0 in front of the lens.

$$h(x) \approx \sqrt{\frac{n}{j\lambda z}} e^{jknz} e^{jkn\frac{x^2}{2z}}. \tag{2.24}$$

Taking the Fourier transform of (2.24), the transform function is obtained

$$H(f_x) = e^{jknz} e^{-j\frac{\pi\lambda z}{n} f_x^2}. \tag{2.25}$$

Let the input field at the plane $z = -d_0 - L(0)$ be $U(x, -d_0 - L_0)$. Its angular spectrum is illustrated as.

$$\tilde{U}(f_x, -d_0 - L(0)) = F\{U(x, -d_0 - L(0))\}. \tag{2.26}$$

The angular spectrum of field at $z = -L(0)$ will be

$$\begin{aligned} \tilde{U}(f_x, -L(0)) &= \tilde{U}(f_x, -d_0 - L(0)) \times H(f_x) \\ &= e^{jknd_0} e^{-j\frac{\pi\lambda d_0}{n} f_x^2} \tilde{U}(f_x, -d_0 - L(0)). \end{aligned} \tag{2.27}$$

The field distribution at the back focal plane of the lens $z = f$ will be proportional to the Fourier transform of the field distribution at the left plane of the lens, as shown in (2.23)

$$\begin{aligned} U(x, f) &= \sqrt{\frac{n}{j\lambda f}} e^{jkn_L\left[f + \frac{x^2}{2f}\right]} e^{jkn_H L(0)} F\{U(x, -L(0))\}_{f_x = \frac{n_L x}{\lambda f}} \\ &= \sqrt{\frac{n_L}{j\lambda f}} e^{jkn_L\left[f + \frac{x^2}{2f}\right]} e^{jkn_H L(0)} e^{jkn_L d_0} e^{-j\frac{\pi\lambda d_0}{n_L}(\frac{n_L x}{\lambda f})^2} \tilde{U}(f_x, -d_0 - L(0))_{f_x = \frac{n_L x}{\lambda f}} \\ &= \sqrt{\frac{n_L}{j\lambda f}} e^{jk[n_L(f + d_0) + n_H L(0)]} e^{ikn_L \frac{x^2}{2f^2}(f - d_0)} \tilde{U}(f_x, -d_0 - L(0))_{f_x = \frac{n_L x}{\lambda f}}. \end{aligned} \tag{2.28}$$

If $d_0 = f$, one of the exponential phase factors outside of the integral becomes 1, it can be further simplified as

$$U(x,f)=\sqrt{\frac{n_L}{j\lambda f}}e^{jk[2n_Lf+n_HL(0)]}\tilde{U}(f_x,-f-L(0))_{f_x=\frac{n_Lx}{\lambda f}}. \tag{2.29}$$

Thus, the Fourier transform without the quadratic phase factor is obtained when the input is placed in the front focal plane and observed on the back focal plane.

2.4 Pupil Function for Blazed Phase Grating

The purpose of the blazed phase grating is to deflect the incident light through a certain angle. A schematic view of the grating is shown in Figure 2.5.

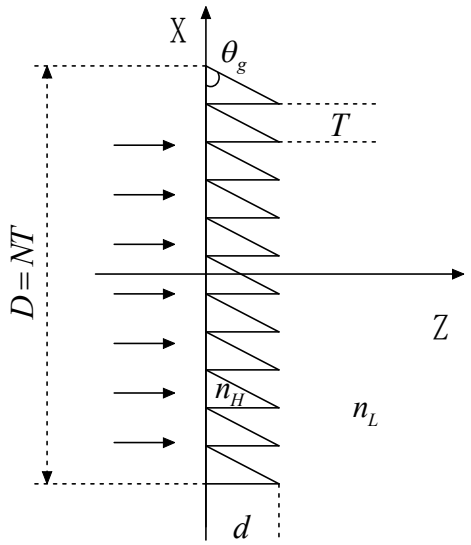

Figure 2.5 Structure of blazed phase grating.

It is composed of N periods of identical triangular wedges with period T, width d and the refractive index n_H. The aperture size is $D=NT$. Assuming a collimated plane wave is launched from its left, after passing through the grating, a pure phase delay will be introduced. Let's consider each period, the unit transfer function is given by

$$\begin{aligned} P_{gu}(x) &= \exp(jkn_H(T/2-x)d/T)\exp(jkn_L(T/2+x)d/T) \\ &= \exp(jkd(n_H+n_L)/2)\exp(-jkd(n_H-n_L)x/T), \end{aligned} \tag{2.30}$$

where $|x| \le T/2$. The periodicity of the structure can be denotes as $P_g(x+T) = P_g(x)$, and therefore we can illustrate the pupil function by a Fourier series

$$P_g(x) = \sum_{m=-\infty}^{\infty} A_m \exp(j2\pi \frac{m}{T} x), \tag{2.31}$$

where the coefficient A_m is expressed by

$$\begin{aligned} A_m &= \frac{1}{T}\int_{-T/2}^{T/2} P_{gu}(x)\exp(-j2\pi \frac{m}{T}x)dx \\ &= \frac{1}{T}\exp(jk\frac{n_H+n_L}{2}d)\int_{-T/2}^{T/2}\exp(-jkd(n_H-n_L)x/T)\exp(-j2\pi\frac{m}{T}x)dx \\ &= \exp(jk\frac{n_H+n_L}{2}d)Sa[\frac{(n_H-n_L)d}{\lambda}+m], \end{aligned} \tag{2.32}$$

where $Sa = \sin(\pi x)/\pi x$. To take the finite aperture into consideration, the pupil function of the grating can be finally written as

$$P_g(x) = \sum_{m=-\infty}^{\infty} A_m \exp(j2\pi \frac{m}{T} x)\cdot G(x/D), \tag{2.33}$$

where the gate function is defined as

$$G(x/D) = \begin{cases} 1, & |x| \le D/2 \\ 0, & else \end{cases}. \tag{2.34}$$

2.5 Summary

In this chapter, we have reviewed the Fresnel and Fraunhofer diffraction. It is based on the fact that any spatial distribution of the complex amplitude of light can be considered a superposition of plane waves[23]. Then the Fourier transforming properties of lenses have been presented. It shows that the field at the lens aperture and the field at the lens focal line forms a Fourier transform pair. As a result, the space Fourier transform

rule is applicable even in the near-field region with the help of the lens. Finally, we have derived the pupil function of the blazed phase gratings which will be employed in the following chapter.

Chapter 3
Initial Design of TD-OFT

3.1 Introduction

As we discussed previously, the conventional TD-OFT normally requires large device size. In addition, it is hard to integrate. Therefore, it is highly demanded to search for an alternative TD-OFT that has the feature of integration compatibility but is less complicated to fabricate and with less cost. In this thesis, a novel planar waveguide TD-OFT by using a combination of waveguide lens and waveguide blazed phase gratings is proposed. Comparing with existing TD-OFT, this device has better performance, lower layout complexity, and more importantly, capable of integration.

This chapter starts with a brief description of the planar waveguide structure. Then a detail theoretic model of TD-OFT is proposed. Next, the reciprocity of the device is investigated. After that, we illustrate the analytical results with several examples and further extend the analysis to demonstrate how the device performance may be affected by the structural parameters or the input pulses. Last, we conclude with a summary of results.

3.2 Planar Waveguide Structure

Planar waveguide structure is based on the ideal of transferring 3D system into a 2D geometry, with the advantage of considerably reduced complexity[24]. The schematic

view is addressed in Figure 3.1. The light is always confined by the slab waveguide in the cross section (x-y plane) while travels along z direction. The effective refractive indices are controlled by the difference of the cladding thickness. Viewing from the top (x-z plane), two different areas are shown: the dark area with thicker cladding and the rest with normal cladding. The dark areas form mesas on top of the normal slab waveguide platform. Therefore, in comparison with the effective refractive index (n_L) of the rest slab waveguide, the dark areas have higher effective refractive index (n_H). The difference of their index ($n_H - n_L$) can be controlled by adjusting the height of the mesa. The shape of the mesa determines its function [25].

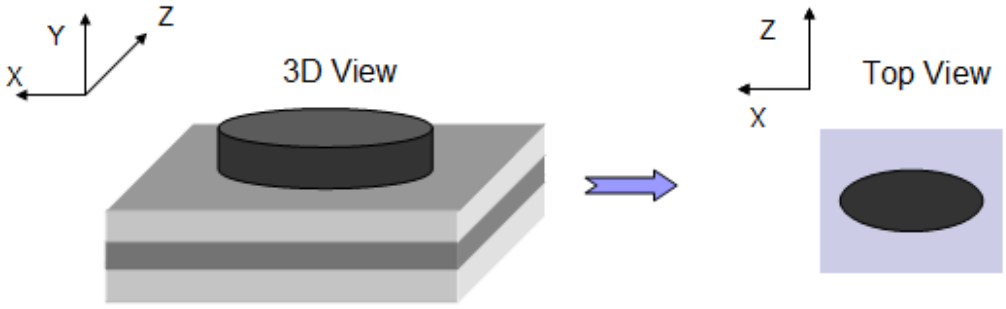

Figure 3.1 Schematic view of waveguide-based structure from both side and top.

3.3 Theoretical Model of TD-OFT

3.3.1 Theoretical Model

The schematic illustration of the TD-OFT together with the coordinate system and the distance used is shown in Fig 3.1. The transverse coordinate is labelled by x axis and propagation direction of the beam is given by z axis. Since the apparatus is uniform

along y direction, only one lateral spatial coordinate is considered. For simplicity, the material dispersion is also ignored in this thesis.

Suppose an ideal ultrafast optical pulse to be processed incident onto the TD-OF from the input waveguide. The first lens with focal distance f_1 transfers the incoming light to a collimated beam. By passing through a blazed phase grating, placed behind the lens, the collimated beam is split up into different frequency components. Each component in the beam can be directly focused into the back focal plane by the second lens L_2. Namely, each single spatial point is located at the position corresponding to the frequency of the incident wave. As a result, the spectrum profile of the ultrafast input signal is mapped into the field distribution in spatial domain. Due to the spatial Fourier transform given by the third lens L_3, with focal distance f_2 , the spectrum profile is converted to a field distribution with the temporal profile. Following the symmetric principle, another lens identical with L_2 and a same diffraction grating are placed there so that the different components are then exactly reconstructed a parallel output beam. Finally, after the last lens, the collimated beam is collected by the output waveguide and converted back into the ultrafast time domain. However, the output temporal profile is now transferred to the replica of the frequency spectrum of the original ultrafast waveform. Thus, the input signal completes its Fourier transform through TD-OFT.

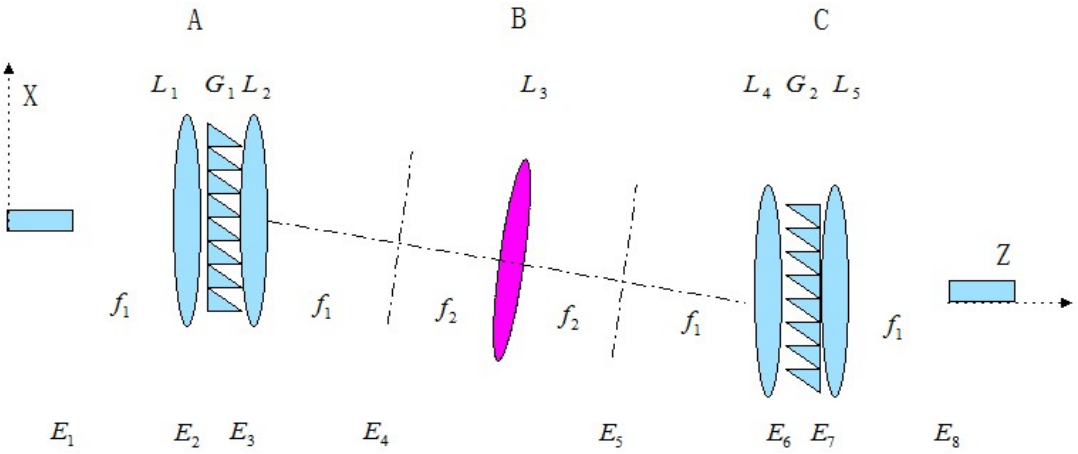

Figure 3.2 Schematic view of TD-OFT system.

The working process of the described setup consists three parts as depicted in Figure 3.3: A) mapping the temporal input pulse to spectrum profile in the spatial domain; B) transferring spectrum profile to temporal waveform in the space by spatial Fourier transform; C) converting the temporal waveform in the spatial plane to the shape of spectrum profile in the time domain. Throughout the process, we can obtain the spectrum profile of the original input pulse in the time domain. A detailed mathematical description of the system will be discussed in the subsequent sections.

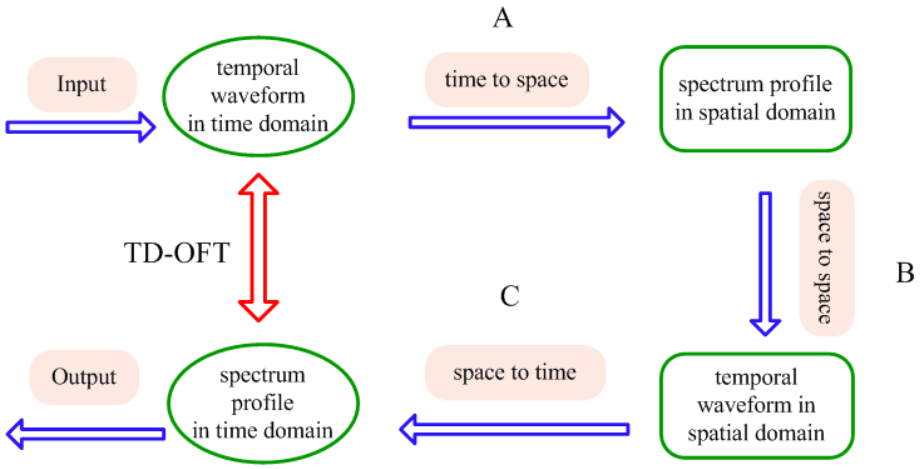

Figure 3.3 Block diagram of TD-OFT pulse processing system.

3.3.2 Mathematical Derivation

Assuming an ultrafast optical pulse with complex amplitude, separable in spatial and temporal dependences, is launched from the input waveguide. Since the guided mode profile in a ridge waveguide is similar to a Dirac impulse function, for simplicity, the input pulse approximates to an ideal point source. Therefore, it can be written as

$$E_1(x_1,t) = \delta(x_1)u_t(t). \tag{3.1}$$

In the frequency domain we have

$$E_1(x_1,t) = \delta(x_1)U(\upsilon), \tag{3.2}$$

where

$$U(\upsilon) = \int_{-\infty}^{+\infty} u_t(t)e^{-j2\pi\upsilon t}dt. \tag{3.3}$$

Here υ is the frequency offset from the central frequency υ_0, i.e. $\upsilon = \upsilon_{opt} - \upsilon_0$, υ_{opt} is the optical frequency variable which can be denotes as $\upsilon_{opt} = c/\lambda$. In our case, the spectral bandwidth of the input pulse is sufficiently narrow so that we have $\upsilon \ll \upsilon_0$.

As Chapter 2 discussed, if the lens is ideal, the field distribution of the incoming beam after the lens is simply the Fourier transform of the pupil function. Note that the phase due to the propagation and the scaling factor are neglected here. Then in the plane of x_2, the collimated field is given by

$$E_2(x_2,\upsilon) = 1 \cdot U(\upsilon). \tag{3.4}$$

After passing through the diffraction grating, the collimated light becomes many sub-beams with wavelength dependent phase shifts by the grating. Mathematically, the

electrical field is multiplied by a pupil function of the grating (see Chapter 2.4) which is repeated here for convenience

$$P_g(x) = \sum_{s=-\infty}^{\infty} A_m \exp(j2\pi \frac{m}{T} x) \cdot rect[x / D], \tag{3.5}$$

where the coefficient A_m is expressed by

$$A_m = \exp(jk \frac{n_H + n_L}{2} d) Sa[\frac{(n_H - n_L)d}{\lambda} + m]. \tag{3.6}$$

Here the grating is made of N identical triangular wedges together with period T, width d, aperture size $D = NT$ and the refractive index n_H. Hence, the field immediately after the grating is derived as

$$\begin{aligned} E_3(x_3, \upsilon) &= E_2(x_3, \upsilon) \cdot P_g(x_3) \\ &= U(\upsilon) \ \exp(jk \frac{n_H + n_L}{2} d) \sum_{m=-\infty}^{+\infty} Sa[\frac{(n_H - n_L)d}{\lambda} + m] \exp(j2\pi \frac{m}{T} x_3) \cdot rect[x_3 / D]. \end{aligned} \tag{3.7}$$

According to the theory of lens described in the previous chapter, the second lens acts as a spatial Fourier transformer which converts the field at the aperture of the grating to its angular spectrum at the focus line. Therefore, the angular spectrum in the focus plane can be written as

$$\begin{aligned} E_4(f_{4x}, \upsilon) &= F\{E_3(x_3, \upsilon)\}_{f_{4x} = \frac{n_L x_4}{\lambda f_1}} \\ &= DU(\upsilon) \ \exp(jk \frac{n_H + n_L}{2} d) \sum_{m=-\infty}^{\infty} Sa[\frac{(n_H - n_L)d}{\lambda} + m] Sa[D(f_{4x} - \frac{m}{T})]. \end{aligned} \tag{3.8}$$

From the relation between the special frequency and the deflected angle shown in Figure 3.4, it is easy to know that

$$\frac{2\pi f_{4x}}{2\pi n_L / \lambda} = \sin\theta \text{ , or } f_{4x} = \frac{n_L \sin\theta}{\lambda}. \tag{3.9}$$

As a result, the diffractive angular spectrum can be expressed as

$$E_4(\theta,\upsilon) = DU(\upsilon)\exp(jk\frac{n_H + n_L}{2}d)\sum_{m=-\infty}^{\infty} Sa[\frac{(n_H - n_L)d}{\lambda} + m]Sa[\frac{Dn_L}{\lambda}(\sin\theta - \frac{m\lambda}{Tn_L})]. \tag{3.10}$$

Moreover, the geometric relation is also obtained

$$\tan\theta = x_4 / f_1. \tag{3.11}$$

If $x_4 \ll f_1$, we have following approximation

$$\sin\theta \approx \tan\theta = \frac{x_4}{f_1}. \tag{3.12}$$

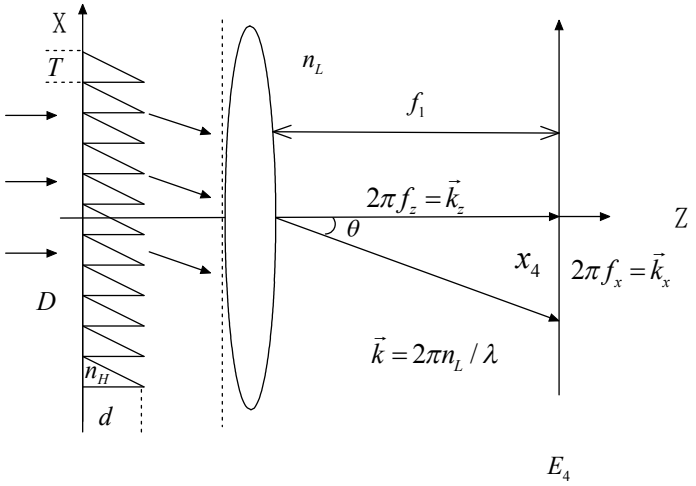

Figure 3.4 Schematic view of lens imaging system.

Therefore, the field in terms of the position coordinate is given by

$$E_4(x_4,\upsilon) = DU(\upsilon)\ \exp(jk\frac{n_H + n_L}{2}d)\sum_{m=-\infty}^{\infty} Sa[\frac{(n_H - n_L)d}{\lambda} + m]Sa[D(\frac{n_L x_4}{f_1\lambda} - \frac{m}{T})]. \tag{3.13}$$

From equation (3.13), the m th order blazing condition for the central wavelength can be written as

$$m = -\frac{n_H - n_L}{\lambda_0} d, \tag{3.14}$$

where λ_0 is the central wavelength. Also we are able to derive the approximate refocusing position x_{4m} for the m th order blazing light

$$x_{4m} \approx \frac{m\lambda f_1}{n_L T}. \tag{3.15}$$

Following (3.12) and (3.15), we can get

$$\theta = \frac{m\lambda}{Tn_L} = \frac{mc}{Tn_L \upsilon}. \tag{3.16}$$

It shows that the deflection angle is a function of the wavelength (or frequency). And thus the beams of different wavelengths will get focused to a different lateral position. In other words, the spatial position depends linearly on the wavelengths, i.e., the focus position of central wavelength yields

$$x_0 \approx \frac{m\lambda_0 f_1}{n_L T} = -\frac{(n_H - n_L) d f_1}{n_L T}. \tag{3.17}$$

Once the grating is met by the blazed condition, here we will use $m = -1$ or $d = \lambda_0 / n_H - n_L$, for central wavelength, any higher order of m always makes the first sinc function in equation (3.13) periodically zero. On the other hand, assume the wavelength offset is much small than the central wavelength, $\Delta\lambda \ll \lambda_0$, then even for other wavelength, the sinc function is still close to zero. As a result, the summation can be dropped off. On the

other hand, θ increases as m increases. Hence, the approximation in (3.12) is no longer valid for large θ. Therefore, the zero value position of the second sinc function in (3.13) will not match with those positions for the first sinc completely. There exists mismatch between the periods of the two sinc functions due to the blazed shape of the grating. As a result, side lobes will appear for high blazed orders[22]. Further more, under the condition $\frac{Dn_L}{\lambda} \to +\infty$, equation (3.13) will be further simplified to

$$\begin{aligned} E_4(x_4,\upsilon) &= DU(\upsilon)\ \exp(jk\frac{n_H+n_L}{2}d)Sa[\frac{Dn_L}{\lambda f}(x_4-\frac{mf_1\lambda}{Tn_L\lambda_0})] \\ &\approx C_1U(\upsilon)\ \delta(x_4-x_0\frac{\upsilon_0}{\upsilon_{opt}}), \end{aligned} \tag{3.18}$$

where $C_{i(i=1,2,..,n)}$ denotes the constant scaling coefficient. As we mentioned before, the modulation frequency is much lower than the carrier frequency, $\upsilon \ll \upsilon_0$, so we will have

$$\frac{\upsilon_0}{\upsilon_{opt}} = \frac{\upsilon_0}{\upsilon_0+\upsilon} = \frac{1}{1+\upsilon/\upsilon_0} \approx 1-\upsilon/\upsilon_0. \tag{3.19}$$

Substituting (3.19) into (3.18) gives

$$\begin{aligned} E_4(x_4,\upsilon) &= C_1U(\upsilon)\ \delta[x_4-x_0(1-\frac{\upsilon}{\upsilon_0})] \\ &= C_1U(\upsilon)\ \delta\left(x_4^{'}+x_0\frac{\upsilon}{\upsilon_0}\right). \end{aligned} \tag{3.20}$$

Here we set the new transverse central axis to be $x_4^{'} = x_4 - x_0$ for convenience.

Performing the integration over frequency of (3.20) obtains the pure spatial distribution in the Fourier plane

$$E_4(x_4^{'}) = C_1 \int_{-\infty}^{+\infty} U(\upsilon)\delta(x_4^{'} + x_0 \frac{\upsilon}{\upsilon_0})d\upsilon$$
$$= C_2 U(-\frac{\upsilon_0}{x_0} x_4^{'}). \tag{3.21}$$

It is clearly shown that the output spatial profile is proportional to the spectrum of the scaled input pulse. In other words, the spectrum profile of the incoming pulse is mapped into the spatial replica in the Fourier plane.

To determine the electrical field in the focus plane of the third lens, a spatial Fourier transform is taken

$$E_5(x_5) = F\{(E_4(x_4))\}_{f_x = \frac{n_L x_5}{\lambda_0 f_2}} = C_2 u_t(-\frac{x_0 n_L x_5}{\upsilon_0 \lambda_0 f_2}). \tag{3.22}$$

Therefore, the spectrum profile is converted to temporal waveform in the spatial domain. After that, the lens L_4 and the second grating G_2 are recombined to form a collimated out beam. That is to say after E5, this part of devise performs an inverse Fourier transformation to obtain the space to time conversion. However, the output radiation now has a new temporal structure which is corresponding to the profile of frequency spectrum.

To account for the remain part of the system, we can use the relation between the deflected angle θ and its corresponded frequency υ to obtain the final results due to the symmetry of whole setup. According to (3.16), after passing through L_4, the spatial profile will be again decomposed to many sub collimated beams with different deflected

angle. With reference to Figure 3.5, the geometric relation as same as equation (3.12) will be achieved.

Therefore, the field in the axis of x_6 can be expressed in terms of θ

$$E_6(\theta) = u_t(-\frac{x_0}{\upsilon_0}\frac{n_L}{\lambda_0 f_2}\theta f_1). \tag{3.23}$$

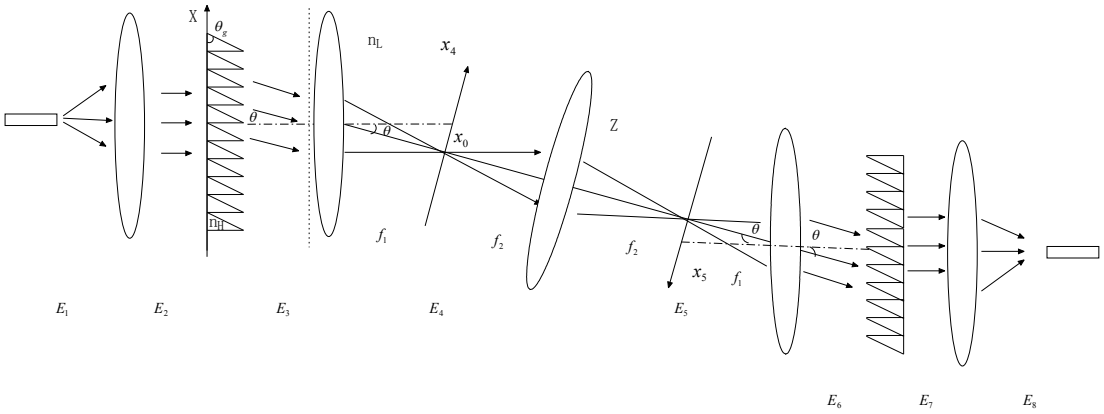

Figure 3.5 TD-OFT apparatus.

The second grating is applied in the inverted geometry so that it reconstructs the light beam with each frequency component. Substituting the inverse transfer function of (3.16) to (3.23) and using equation (3.19) gives the electrical field immediately after the grating

$$E_7(\upsilon) = u_t(\frac{x_0 m\upsilon}{\upsilon_0^2 T})\cdot 1. \tag{3.24}$$

Taking the inverse temporal Fourier transform of (3.24), the output waveform in the time domain is given by

$$E_8(t, x_8) = \int_{-\infty}^{+\infty} u_t(\frac{x_0 m\upsilon}{\upsilon_0^2 T}) e^{2\pi\upsilon t} d\upsilon = U(\frac{\upsilon_0^2 T}{x_0 m}t)\delta(x_8). \tag{3.25}$$

Reference to (3.25), it is of interest to note that the output temporal waveform is proportional to the spectrum shape $U(\upsilon)$ ($\upsilon = \frac{\upsilon_0^2 T}{x_0 m} t$) of the input waveform. The whole device plays a role as a time domain Fourier transformer

3.4 Reciprocity in TD-OFT

The reciprocity in wave propagation is a general theorem which has been verified theoretically and experimentally [26, 27]. Typically, this refers to the symmetry of propagation under the interchange of the source and the observer. As it is proved that in the case of lossless waveguide the theorem is satisfied [28, 29], reciprocity is also applicable in TD-OFT.

If the output wave is launched from the right-hand output waveguide to the left-hand input waveguide, the wave will completely retrace the incidence path and the original input signal can be finally obtained. As a result, the TD-OFT can be formulated mathematically in a reversed way through the reciprocity symmetry. For simplicity, only the results indicating the propagation from the output to the axis of x_5 are summarized here. As sketched in Figure 3.6, $E'_{i(i=8,7...,5)}$ is denoted as the electrical field in a specific plane. As we derived previously in (3.25), the output waveform is given by

$$E'_8(x_8, t) = U(\frac{\upsilon_0^2 T}{x_0 m} t)\delta(x_8). \tag{3.26}$$

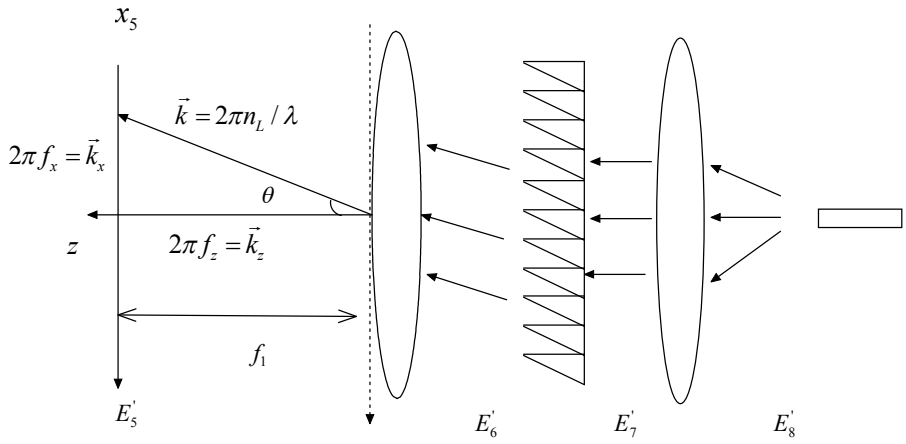

Figure 3.6 Output waveform is launched from right-hand waveguide to the left-hand.

A collimated beam is obtained by passing the lens. It can be expressed in the frequency domain

$$E_7^{'}(x_7,\upsilon) = u_t(\frac{x_0 m\upsilon}{\upsilon_0^2 T})\cdot 1. \tag{3.27}$$

The diffraction grating is applied via multiplying the transfer function

$$E_6^{'}(x_6,\upsilon) = E_7^{'}(x_7,\upsilon)\cdot P_g(x_7). \tag{3.28}$$

Through the spatial Fourier transform, the field immediately after the lens is derived as

$$E_5^{'}(f_{5x},\upsilon) = Du_t(\frac{x_0 m\upsilon}{\upsilon_0^2 T})\exp(jk\frac{n_H + n_L}{2}d)\sum_{m=-\infty}^{+\infty} Sa[\frac{(n_H - n_L)d}{\lambda} + m]Sa[D(f_{5x} - \frac{m}{T})]. \tag{3.29}$$

Under the approximations described previously, it will be further simplified in term of spatial coordinate

$$E_5^{'}(x_5,\upsilon) = C_1^{'}u_t(\frac{x_0 m\upsilon}{\upsilon_0^2 T})\ \delta(\frac{\upsilon_0}{x_{50}}x_5^{'} + \upsilon). \tag{3.30}$$

where $x_5^{'} = x_5 - x_{50}$, x_{50} is the focus position of central wavelength. It is easily to proved the following relation

$$x_{50} = x_0 \approx \frac{m\lambda_0 f_1}{n_L T}. \tag{3.31}$$

The spatial field distribution, corresponding to the plane of x_5 is given by

$$\begin{aligned} E_5'(x_5') &= C_1' \int_{-\infty}^{+\infty} u_t(\frac{x_0 m\upsilon}{\upsilon_0^2 T})\ \delta(\frac{\upsilon_0}{x_{50}} x_5' + \upsilon) d\upsilon \\ &= C_2' \int_{-\infty}^{+\infty} u_t(\frac{x_0 m\upsilon}{\upsilon_0^2 T})\ \delta(\frac{m x_5'}{\upsilon_0 T} + \frac{x_0 m}{\upsilon_0^2 T}\upsilon) d\,\frac{x_0 m}{\upsilon_0^2 T}\upsilon \\ &= C_2' u_t(-\frac{m x_5'}{\upsilon_0 T}). \end{aligned} \tag{3.32}$$

Using (3.17) to replace m, it becomes

$$E_5'(x_5') = C_2' u_t(-\frac{x_0 n_L x_5'}{\lambda_0 \upsilon_0 f_2}). \tag{3.33}$$

Comparing with equation (3.22), we have

$$E_5'(x_5) = E_5(x_5). \tag{3.34}$$

It is clearly shown the field distribution which results from the input pulse emerging from the left is identical to the one which is contributed by the output waveform launching from the right. Therefore, with reciprocity theorem, the theoretic model of TD-OFT is verified.

3.5 Implementation by Analytical Formulations

As we stated above, the input pulse can be transformed to its spectrum profile in time domain as long as the lenses and gratings are properly designed. To prove the initial design concept, three different examples are implemented by analytical formulations.

3.5.1 Gaussian Pulse

Consider a Gaussian input pulse centered at υ_0 as shown in Figure 3.7

$$E_1(x_1,t) = \delta(x_1)\exp(-\frac{t^2}{\tau^2}), \tag{3.35}$$

with pulse duration $\tau = 10\,\text{ps}$. The Fourier transform spectrum of the pulse is also Gaussian shape

$$E_1(x_1,\upsilon) = \tau\sqrt{\pi}\delta(x_1)\exp[-(\tau\pi\upsilon)^2], \tag{3.36}$$

where $\upsilon = \upsilon_{opt} - \upsilon_0$.

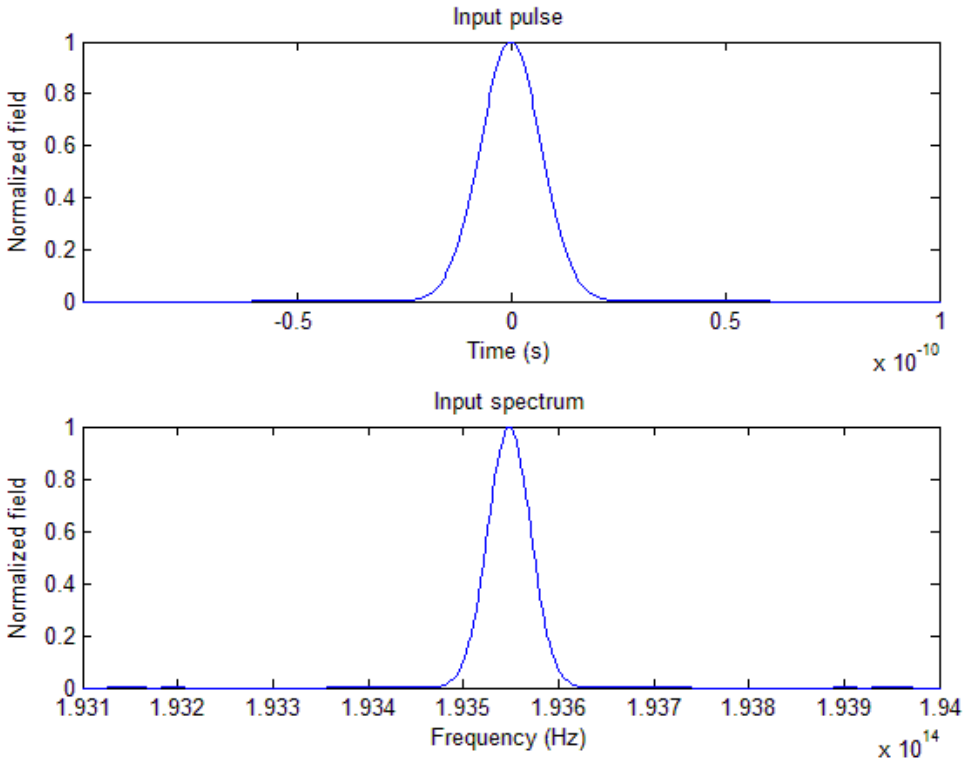

Figure 3.7 Gaussian pulse with duration $\tau = 10\,\text{ps}$.

With equation (3.13), we can derive the resulting spatial distribution in the Fourier plane x_4

$$E_4(x_4,\upsilon) = D\tau\sqrt{\pi}\exp[-(\tau\pi\upsilon)^2]\exp(jk\frac{n_H+n_L}{2}d)\sum_{m=-\infty}^{\infty} Sa[\frac{(n_H-n_L)d}{\lambda}+m]Sa[D(\frac{n_L x_4}{f_1\lambda}-\frac{m}{T})]. \tag{3.37}$$

It is worth mentioning that this equation leads to several important observations.

1) When the grating is satisfied with the blazed condition, i.e., $m=-(n_H-n_L)d/\lambda_0=-1$, as for central wavelength, any other high order of m will leads the first sinc function periodically zero.

2) The second sinc function will approach the delta function only if the argument $N\frac{Tn_L}{f_1}$ ($D=NT$) is extremely large. Hence, to get better shape performance, we need to make it as large as possible.

3) On the other hand, the spectra resolution of the setup is determined by

$$\frac{\Delta x}{\Delta\lambda}=\frac{mf_1}{Tn_L}, \tag{3.38}$$

which means the higher resolution requires smaller $\frac{Tn_L}{f_1}$. For this reason, we should find the optimum $\frac{Tn_L}{f_1}$ to meet the trade-off between the waveform similarity and the spectra resolution.

By comparison, the frequency spectrum and the spatial distribution in the plane of x_4 is displayed in a same coordinate after scaling and normalization, as shown in Figure 3.8. For the four distributions, each with the central wavelength $\lambda_0=1.55um$, but with

different grating apertures, i.e., $D = 5mm, 13mm, 21mm, 29mm$, respectively. Other structure parameters are summarized in Table 2.1.

Table 3.1 Initial design of structure parameters for TD-OFT.

Structure parameters	**value**
Slab effective refractive index n_L	3.2
Mesa effective refractive index n_H	3.6
Diffraction grating period T (μm)	3.88
Diffraction grating width d (μm)	3.88
Diffraction order m	-1
Lens focal length f_1, f_2 (μm)	628

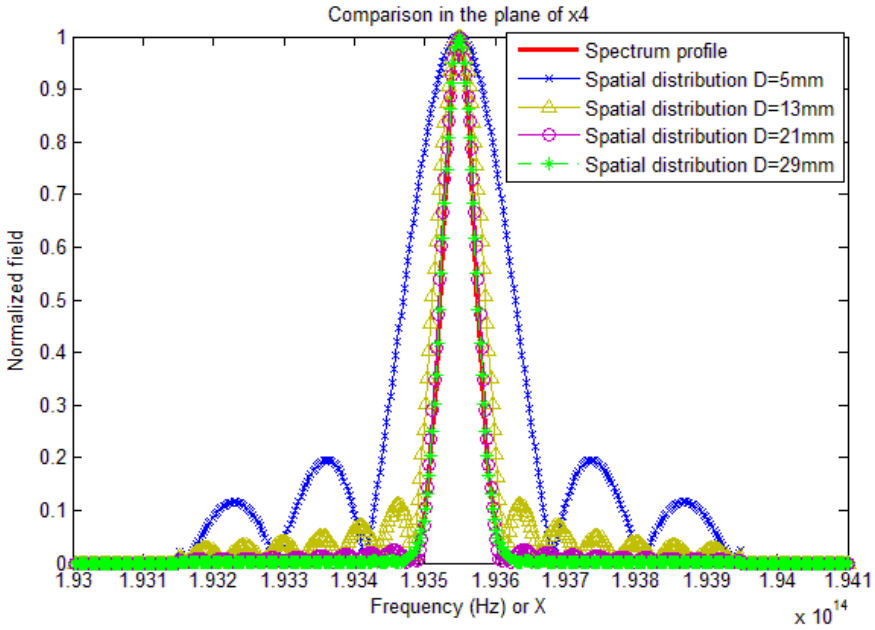

Figure 3.8 Comparison between the spatial distributions of different grating apertures and ideal spectrum profile in the plane of x_4.

The figure is clearly shown that when the aperture is small, the side-lobe level is high due to the diffraction effect. While the aperture increases, the sinc function will get closer to the delta function. As a result, the spatial distribution is approaching its corresponding spectrum. In order to describe the similarity of two different profiles and evaluate performance of the device , the similarity coefficient is defined as follows

$$Simi(\tau)=\frac{\int_{-\infty}^{\infty} f_1(t)f_2(t+\tau)dt}{\sqrt{\int_{-\infty}^{\infty} f_1(t)^2 dt \int_{-\infty}^{\infty} f_2(t)^2 dt}}. \tag{3.39}$$

According to (3.39), one obtains the similarity of each distribution as shown in Table 3.2. The spectra resolution in the focus plane can be demonstrated as $\frac{\Delta x}{\Delta\lambda}=\frac{60\text{nm}}{0.8\text{nm}}=75$

Table 3.2 The aperture value and corresponding similarity of E_4.

Aperture	5mm	13mm	21mm	29mm
Similarity	75.98%	96.65%	99.81%	100%

Following the spatial Fourier transform, the spatial profile behind the third lens, namely E_5, is obtained as illustrated in Figure 3.9 and the corresponding similarity is expressed in Table 3.3. It is clearly shown that the similarity also increases with an increase of the aperture.

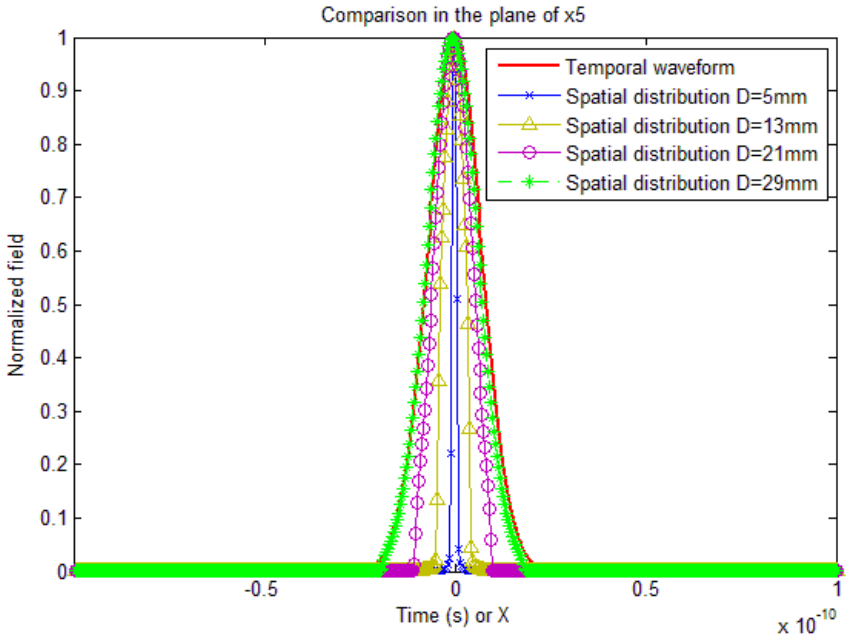

Figure 3.9 Comparison between the spatial distributions of different grating apertures and ideal temporal waveform in the plane of x_5.

Table 3.3 The aperture value and corresponding similarity of E_5.

Aperture	5mm	13mm	21mm	29mm
Similarity	37.77%	76.04%	95.59%	99.79%

Consider a pulses with shorter pulse width, for example τ=100fs. To get the similarity 100% at x_4 and 99% at x_5, as shown in Figure 3.10, the apertures is only required about 456μm. It is clearly to show that the shorter pulse (larger bandwidth) can have smaller aperture size.

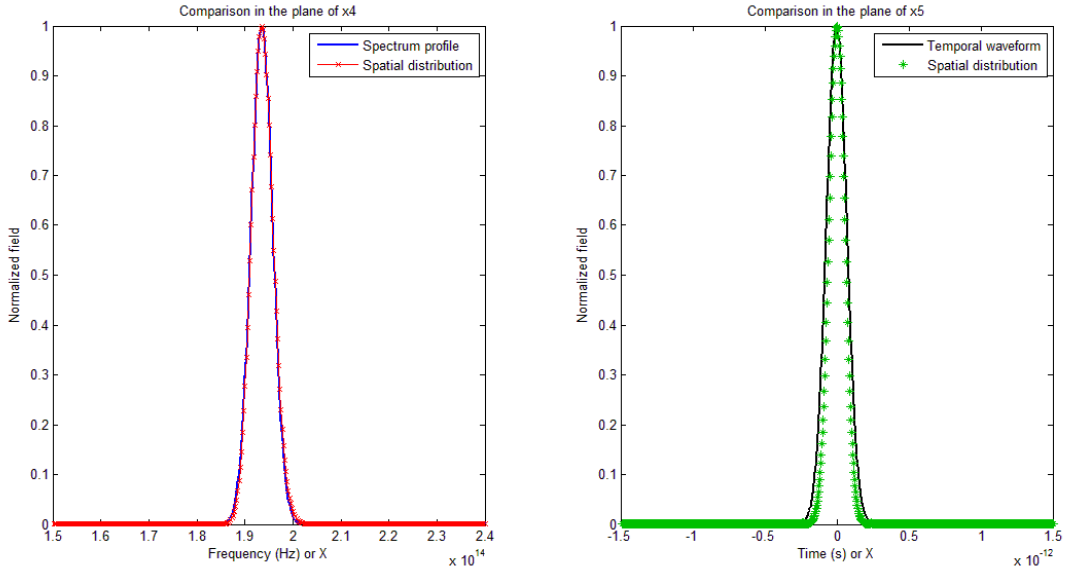

(a) (b)

Figure 3.10 For Gaussian pulse with duration τ=100fs. (a) Comparison between the spatial distribution and ideal temporal waveform in the plane of x_4. (b) Comparison between the spatial distribution and ideal temporal waveform in the plane of x_5.

For comparison, let's choose the input pulse width τ=50fs, 100fs, 200fs, respectively. With the same structure mentioned above, we can get the amplitude distributions of E_4 and E_5 for each signal. From Figure 3.11, one can notice if the input is a shorter temporal duration optical pulse, then the width of spatial profile in the focus plane of x_4, is widen due to the broader spectrum. As a result, as shown in Figure 3.12, in

the Fourier plane of x_5, the field distribution ranges spatially over a narrower distance. Figure 3.13 shows the final temporal output fields for three pulses. They are compressed in time domain and proportional to the corresponding scaled spectrum profile.

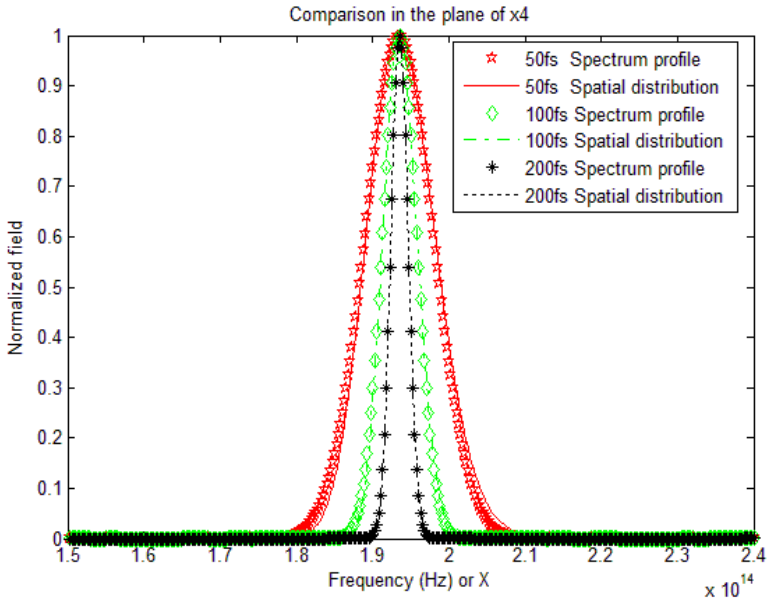

Figure 3.11 Comparison between the spatial distributions of different pulse durations and ideal spectrum profile in the plane of x_4.

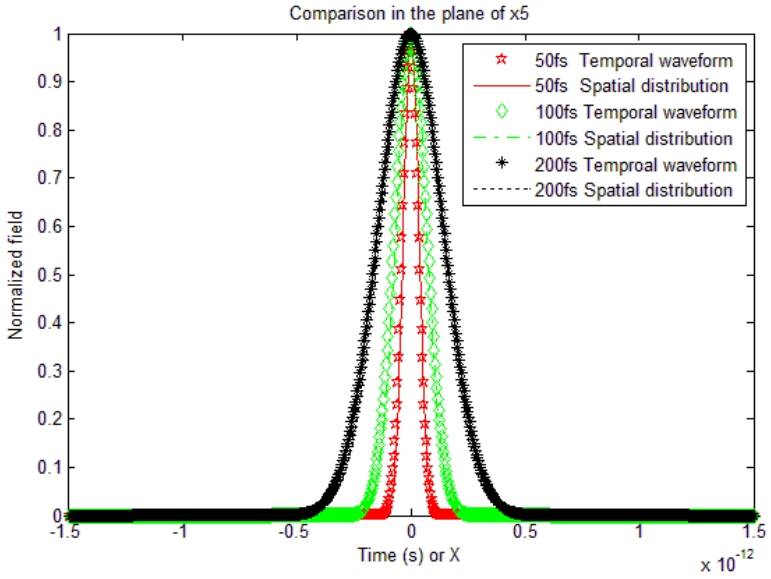

Figure 3.12 Comparison between the spatial distributions of different pulse durations and ideal temporal waveform in the plane of x_5.

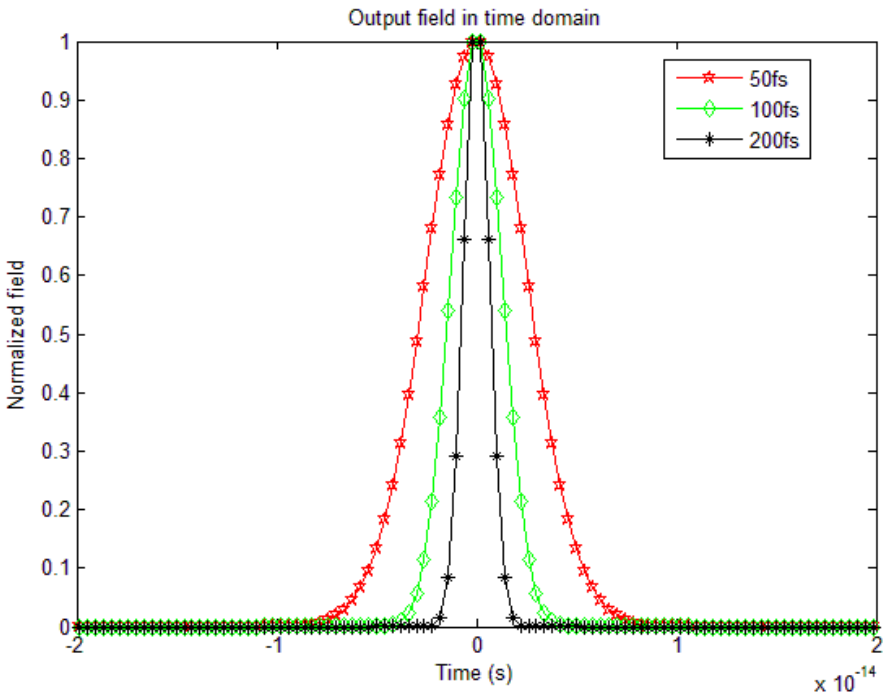

Figure 3.13 Temporal output fields for different pulse durations with input Gaussian pulse.

3.5.2 Square Pulse

As another example, suppose a square pulse centered at $\lambda_0 = 1.55$um with duration $T_0 = 10$ps as shown in Figure 3.14(a). Its temporal part, $u_t(t)$, is then described as

$$u_t(t) = rect(-\frac{t}{T_0}), \tag{3.40}$$

It's frequency spectrum, shown in Figure 3.14(b), is given by

$$U(\upsilon) = T_0 \sin c(T_0 \upsilon). \tag{3.41}$$

The structure parameters are based on Table 3.1 with the aperture D=11.4mm. Following the same procedure we discussed in the previous section, we can get the spatial

distribution in the plane of x_4 and x_5 given by Figure 3.14(c) and Figure 3.14(d) , respectively.

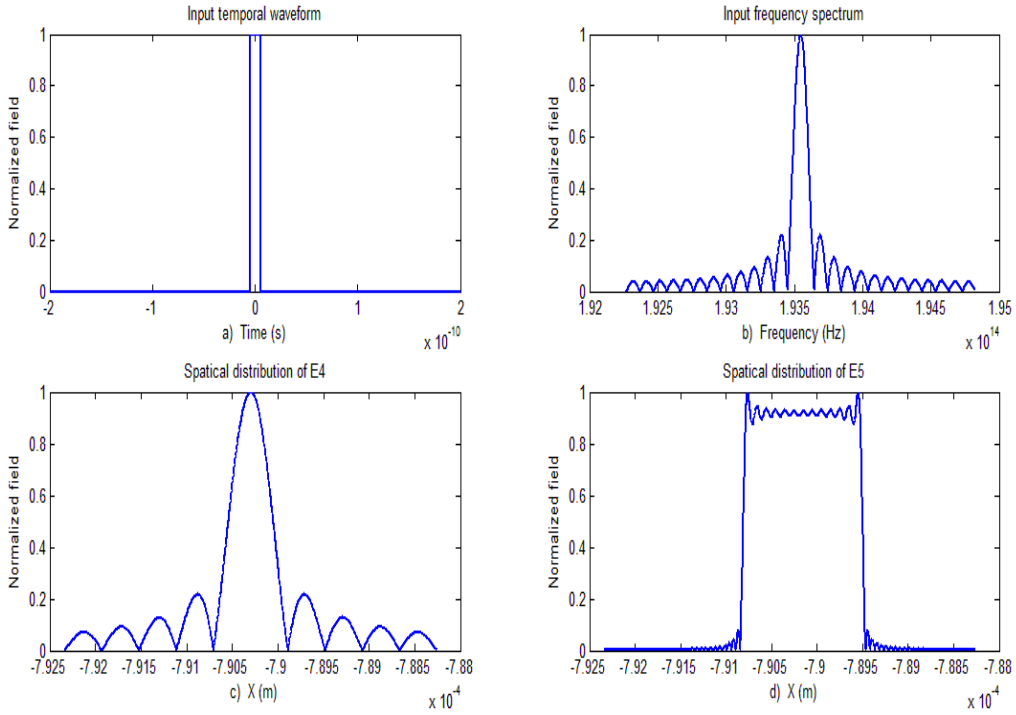

Figure 3.14 For square pulse with duration τ =10 ps. a) Input pulse of square waveform. b) Its frequency spectrum. c) Spatial distribution in the plane of x_4. d) Spatial distribution in the plane of x_5.

To compare with the input frequency spectrum or input temporal waveform, again, we show the scaled spatial distribution E_4 or E_5 in the same coordinate. As Figure 3.15 and Figure 3.16 demonstrate, both of them are agreed with the corresponding input. The similarity is calculated as 99.96% for E_4 , 99.78% for E_5.

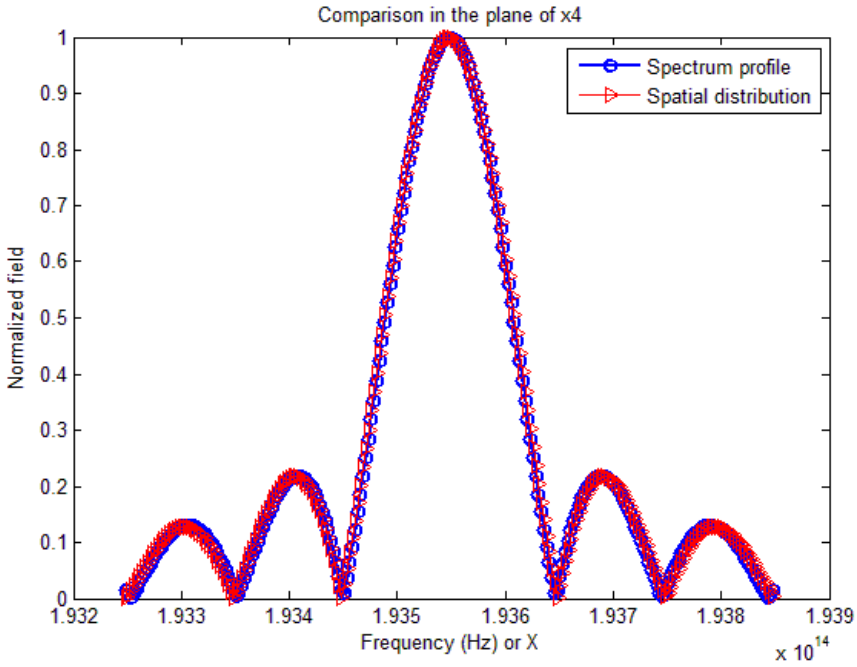

Figure 3.15 Comparison between the spatial distribution and ideal spectrum profile in the plane of x_4 with input square pulse.

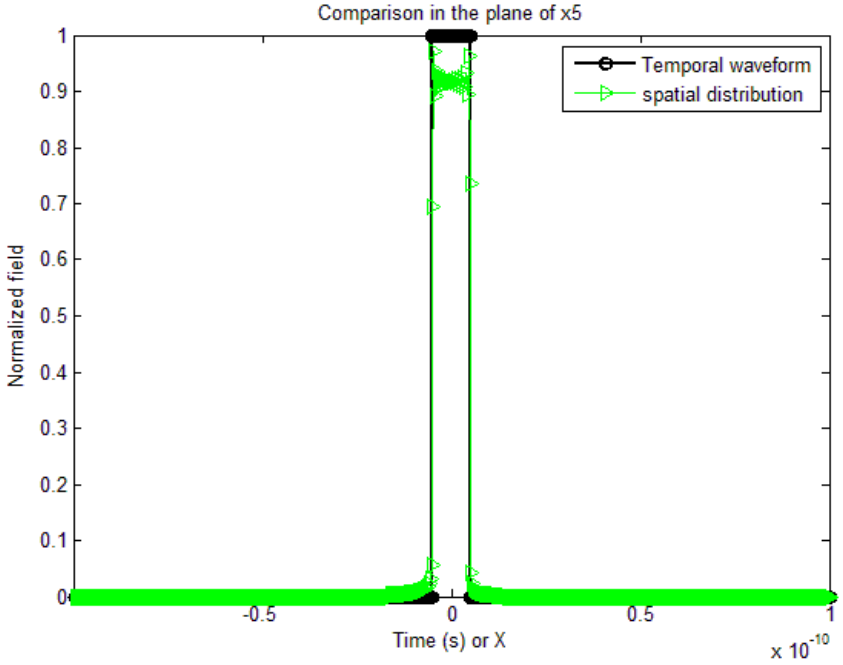

Figure 3.16 Comparison between the spatial distribution and ideal temporal waveform in the plane of x_5 with input square pulse.

The final output waveform in the time domain is given by Figure 3.17.

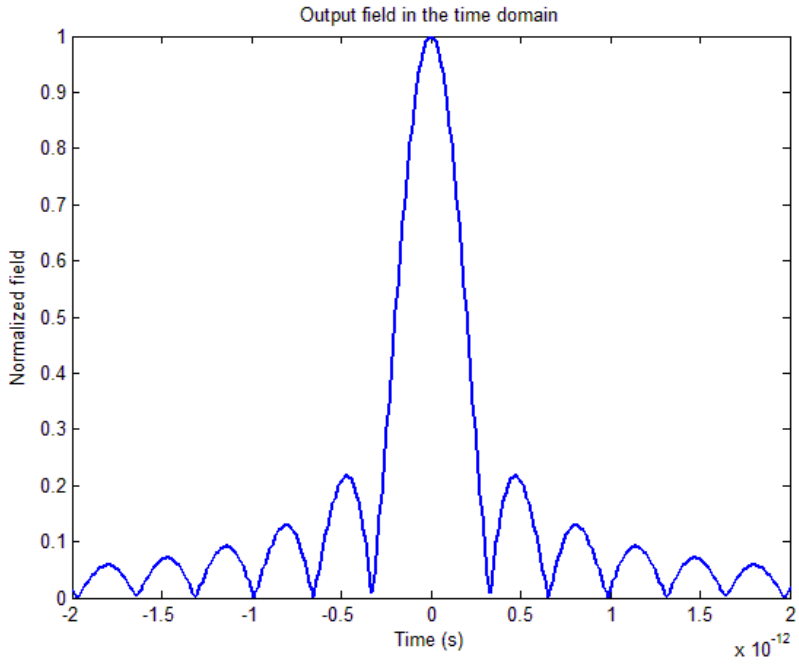

Figure 3.17 Temporal output field for different pulse durations with input square pulse.

3.5.3 Square Pulse Train

One application of the TD-OFT is in the generation of pulse train or pulse sequences. Here we discuss the square input pulse train with duration $T_0 = 10^{-12}$ s , see in Figure 3.18. The comparison between the input spectrum profile and the spatial distribution of E_4 , or between the original temporal waveform and the spatial distribution of E_5 , is shown in Figure 3.19 , Figure 3.20 respectively. However, to get the similarity as high as 98%, the aperture has to be enlarged to 532 mm. This is based on the fact that there are much more details (or high frequency components) including in the

spectrum profile of the pulse train compared to the single pulse. Therefore, in this case, TD-OFT can work only under the condition of a larger aperture.

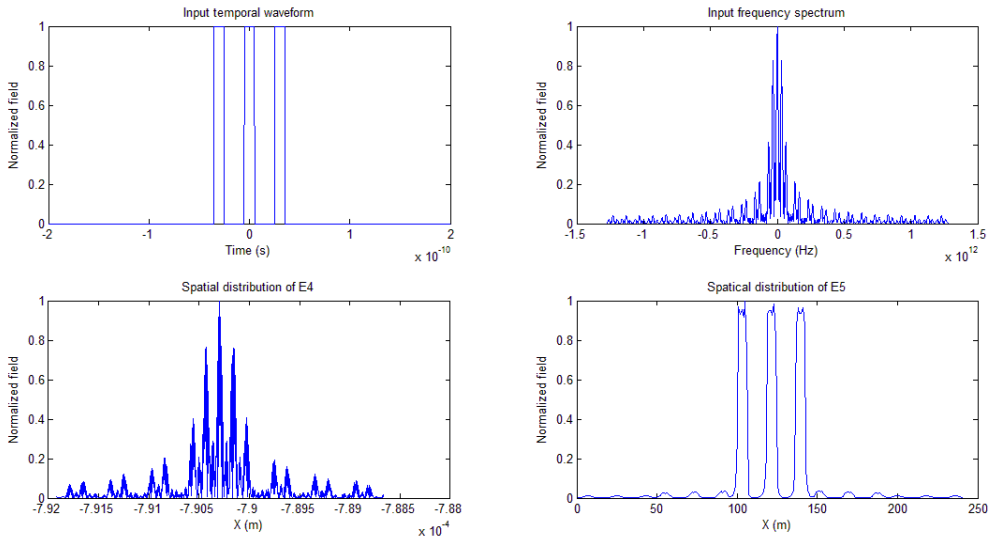

Figure 3.18 For square pulse train. a) Input pulse train. b) Its frequency spectrum. c) Spatial distribution in the plane of x_4. d) Spatial distribution in the plane of x_5.

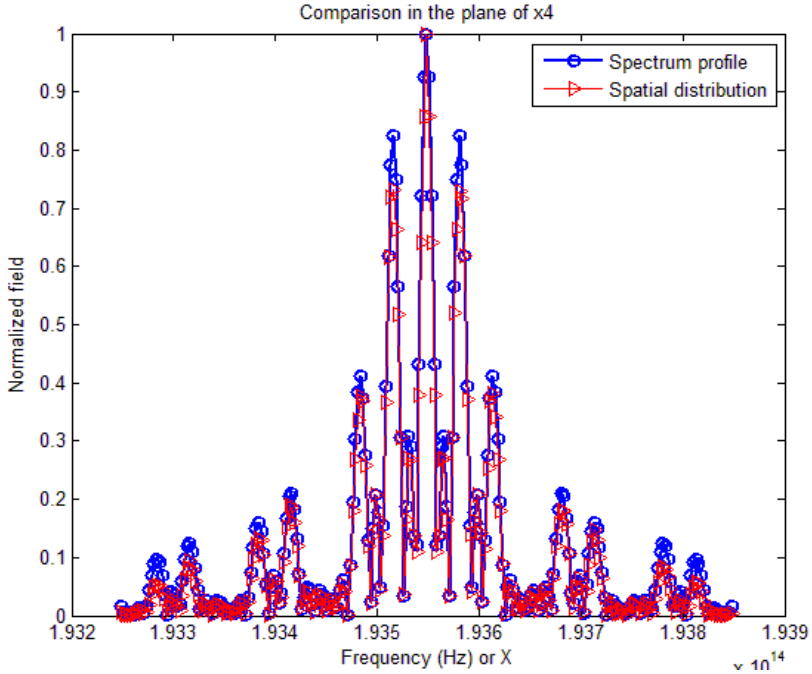

Figure 3.19 Comparison between the spatial distribution and ideal spectrum profile in the plane of x_4 with input square pulse train.

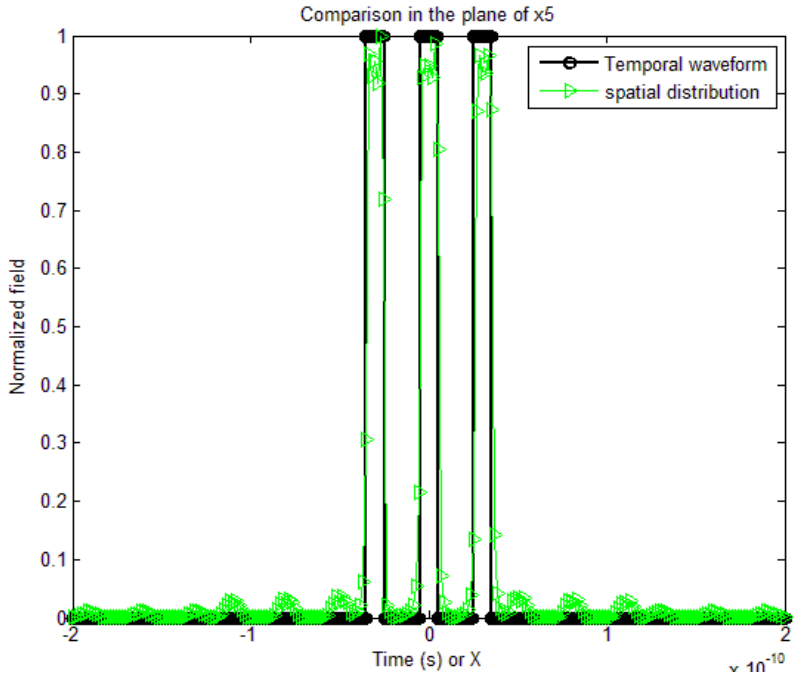

Figure 3.20 Comparison between the spatial distribution and ideal temporal waveform in the plane of x_5 with input square pulse train.

3.6 Summary

In this chapter, we have proposed a new design for planar waveguide TD-OFT by combining waveguide lenses and waveguide blazed phase gratings. Three examples have been chosen to study how the device performance is affected by the structural parameters and the input pulses. In order to evaluate the performance, the similarity coefficient has been defined. Namely, larger similarity coefficient is corresponding to better device performance. The results show that the similarity increases as the device aperture increases. For the input pulse, under the circumstance of same similarity, the shorter temporal pulse duration (larger bandwidth) needs smaller aperture size.

Chapter 4
Improved Design and Numerical Verification by Extension of BPM Simulation

4.1 Introduction

The fundamental design concept was proposed in the previous chapter. However, it is based on the assumption that the input is a Dirac function and the lens is ideal. Although it provides an ideal pulse shaping response and simplifies the mathematical derivation, it is not practical. In real case, the waveguide mode is launched from the input port instead of the point source. And, the limited aperture of the lens can introduce non-ideal spatial Fourier transform. Also, the discontinuity of the grating's corners may introduce extra diffraction. Taking all these limitations into account, a more precise numerical simulation such as Beam Propagation Method (BPM) has to be carried out to verify the design.

This chapter is organized in the following way. First, the Extension of BPM (EX-BPM) is described in section 4.2. Then, an improved design of waveguide lens based on scalar wave propagation and paraxial approximation is presented in section 4.3. After that, the performance of the design is evaluated with several examples, i.e., Gaussian pulse and raised cosine pulse. For the sake of verification, the reciprocity theorem is also applied in the simulation. In section 4.5, we summarize.

4.2 Extension of BPM in Time Domain

4.2.1 Beam Propagation Method

Beam propagation method (BPM) based on finite-difference (FD) scheme is the most widely spread numerical tool in the study of electromagnetic field propagation in optical waveguides and photonic integrated circuits.

For the sake of simplicity, the two-dimensional case is treated. Let's start with the scalar Helmholtz equation for the electric field transverse component E [30-32]

$$\frac{\partial^2 E}{\partial x^2} + \frac{\partial^2 E}{\partial z^2} + k_0^2 n^2(x) E = 0, \tag{4.1}$$

where $n(x)$ is the refractive index, k_0 is the wave number in free space and λ is the wavelength. By assuming the wave travels along z direction without reflection, the field can be expressed as the combination of a slowly varying envelope and a fast-oscillating phase term

$$E(x,z) = U(x,z) e^{-jk_0 n_0 z}, \tag{4.2}$$

where n_0 is the reference refractive index, substituting (4.2) into (4.1), the one way wave equation can be written as follows

$$\frac{\partial^2 U}{\partial z^2} - 2jk_0 n_0 \frac{\partial U}{\partial z} + \frac{\partial^2 U}{\partial x^2} + k_0^2 (n^2 - n_0^2) U = 0. \tag{4.3}$$

To derive the equation for the wide-angle BPM, the (4.3) can be reduce to

$$\frac{\partial U}{\partial z} = -jk_0 n_0 (\sqrt{1+X} - 1) U, \tag{4.4}$$

where $X = \frac{1}{k_0^2 n_0^2}\left[\frac{\partial^2}{\partial x^2} + k_0^2(n^2 - n_0^2)\right]$.

Given the field at the propagation distance z, the solution to (4.4) at $z + \Delta z$ is given by

$$U(z+\Delta z) = \exp\left[-jk_0 n_0(\sqrt{1+X} - 1)\right]U(z). \tag{4.5}$$

Note that $\sqrt{1+X}$ is the square root operator, it should be amended to direct numerical solution with rationalization. For this purpose, the efficient multi-step method based on Padé approximation is utilized [33, 34].

$$\sqrt{1+X} \approx 1 + \sum_{i=1}^{p} \frac{a_{i,p} X}{1 + b_{i,p} X}, \tag{4.6}$$

where

$$a_{i,p} = \frac{2}{2p+1}\sin^2\left(\frac{i\pi}{2p+1}\right), \tag{4.7}$$

$$b_{i,p} = \cos^2\left(\frac{i\pi}{2p+1}\right). \tag{4.8}$$

The multi-step scheme is obtained by rewriting (4.5) as

$$\begin{aligned} U(z+\Delta z) &= \exp\left(-jk_0 n_0 \sum_{i=1}^{p} \frac{a_{i,p} X}{1 + b_{i,p} X}\Delta z\right)U(z) \\ &= \prod_{i=1}^{p} \exp\left(-jk_0 n_0 \Delta z \frac{a_{i,p} X}{1 + b_{i,p} X}\right)U(z) \\ &= \prod_{i=1}^{p} \frac{1 - \frac{jk_0 n_0 \Delta z}{2}\frac{a_i X}{1 + b_i X}}{1 + \frac{jk_0 n_0 \Delta z}{2}\frac{a_i X}{1 + b_i X}}U(z). \end{aligned} \tag{4.9}$$

From which the ith step takes the form

$$U[z+i\Delta z/p]=\exp\left(-jk_0n_0\Delta z\frac{a_{i,p}X}{1+b_{i,p}X}\right)U[z+(i-1)\Delta z/p]. \tag{4.10}$$

The Crank-Nicholson scheme for the exponential function is used, which yields

$$\begin{aligned}U[z+i\Delta z/p]&=\frac{1-\frac{jk_0n_0\Delta z}{2}\frac{a_{i,p}X}{1+b_{i,p}X}}{1+\frac{jk_0n_0\Delta z}{2}\frac{a_{i,p}X}{1+b_{i,p}X}}U[z+(i-1)\Delta z/p]\\&=\frac{1+\tau_oX}{1+\tau_pX}U[z+(i-1)\Delta z/p],\end{aligned} \tag{4.11}$$

where

$$\tau_o=b_{i,p}-\frac{jk_0n_0\Delta z}{2}a_{i,p}, \tag{4.12}$$

$$\tau_p=b_{i,p}+\frac{jk_0n_0\Delta z}{2}a_{i,p}. \tag{4.13}$$

Applying the second-order FD formula to (4.11), we can relate the electric field at $m\Delta z+i\Delta z/p$, i.e., $U^{m+i/p}$, to the field at $m\Delta z+(i-1)\Delta z/p$, i.e., $U^{m+(i-1)/p}$ by the following expression

$$\tau_0U_{i-1}^{m+i/p}+\tau_0QU_i^{m+i/p}+\tau_0U_{i+1}^{m+i/p}=\tau_pU_{i-1}^{m+(i-1)/p}+\tau_pBU_i^{m+(i-1)/p}+\tau_pU_{i+1}^{m+(i-1)/p}, \tag{4.14}$$

where

$$Q=\left[\frac{k_0^2n_0^2\Delta x^2}{\tau_o}-2+\Delta x^2k_0^2\left(\left(\frac{n_i^{m+i/p}+n_i^{m+(i-1)/p}}{2}\right)^2-n_0^2\right)\right], \tag{4.15}$$

$$B=\left[\frac{k_0^2n_0^2\Delta x^2}{\tau_p}-2+\Delta x^2k_0^2\left(\left(\frac{n_i^{m+i/p}+n_i^{m+(i-1)/p}}{2}\right)^2-n_0^2\right)\right]. \tag{4.16}$$

4.2.2 Extension of BPM

As outlined previously, the conventional BPM is based on the formulations in the frequency domain and therefore not directly applicable for the time domain analysis of pulse propagation [35-37]. Although the finite-differences time-domain (FDTD) method is the powerful technique for simulation of temporally varying waveforms in the guided-wave devices, it requires huge computer resources due to the small time step size, and more importantly, it is not suitable for optically large structures. To improve the efficiency, an extension of beam propagation method (EX-BPM) has been developed [38]. This approach based on the linear optical structure can describe the propagation of optical fields in the time domain with high precision.

In a linear optical structure, the propagation of pulse can be linear decomposed into different frequencies and each one independently propagates with the well established BPM technique. A pulse at the time t can be indicated as a superposition of monochromatic waves.

$$u_t(x,z,t) = \int_{-\infty}^{\infty} \tilde{U}(x,z,\upsilon) e^{-2\pi j\upsilon t} d\upsilon, \tag{4.17}$$

where $\tilde{U}(x,z,\upsilon) = \int_{-\infty}^{\infty} u_t(x,z,t) e^{-2\pi j\upsilon t} d\upsilon$, $\upsilon = c/\lambda$, c is the speed of light in the free space and λ is the wavelength. Assume that an input pulse at $t = 0$ is launched from $z = 0$ into the guiding structure along $\hat{z}$ direction. Numerically, (4.17) is discredited as

$$u_0(x,0,t) = \sum_{m=-\infty}^{\infty} U(x,0,\upsilon_m) e^{-2\pi j\upsilon_m t}, \tag{4.18}$$

where $U(x,0,\upsilon_m)=\tilde{U}(x,z,\upsilon_m)\Delta\upsilon$, $\Delta\upsilon=1/T$, T is the time length of window and $\upsilon_m=\upsilon_0+m\Delta\upsilon,\upsilon_0$ is the central carrier frequency. For each frequency component, the function $U(x,0,\upsilon_m)$ is propagated along the guiding structure with the ordinary BPM which can be represented as

$$U(x,\Delta z,\upsilon_m)=\exp\left(j\sqrt{\partial^2/x^2+k_m^2}\right)U(x,0,\upsilon_m), \tag{4.19}$$

where the propagation constant is defined by $k_m=2\pi\upsilon_m/c$. The optical field at the desired distance z is obtained when we repeat the operation in (4.19). Considering the structure is optically linear, no new frequencies are generated. Therefore the pulse profile at the time t can be reconstructed from the inverse Fourier Transform

$$u_t(x,z,t)=\sum_{m=-\infty}^{\infty}U(x,z,\upsilon_m)e^{-2\pi j\upsilon_m t}. \tag{4.20}$$

4.3 Design of Waveguide Lens

4.3.1 Mathematical Derivation

In chapter 2, we discussed the conventional lens. Although it is thin, it has a larger focal distance. Here, an improved waveguide lens is proposed [25] [22]. The schematic diagram with an aperture D is illustrated in Figure 4.1.

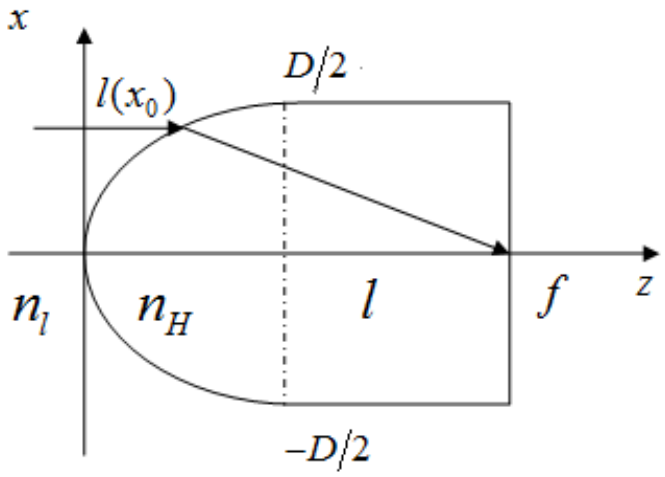

Figure 4.1 A schematic diagram of a lens structure.

The refractive indices inside and outside the lens structure are denoted by n_L and n_H, respectively. As shown in the sketch, the lens should be shaped in such a way that makes the collimated light illuminating from left to right focused at the distance of f or vice versa. According to the ray optics theory, the optical paths of the rays in the collimated beam should be all equal

$$n_H f = n_L l(x_0) + n_H \sqrt{[f - l(x_0)]^2 + x_0^2}. \tag{4.21}$$

It can be rewritten in the following form

$$\frac{[l(x_0) - a]^2}{a^2} + \frac{x_0^2}{b^2} = 1, \tag{4.22}$$

where

$$a = \frac{n_H f}{n_L + n_H}, \tag{4.23}$$

$$b = f\sqrt{\frac{n_H - n_L}{n_H + n_L}}. \tag{4.24}$$

It is shown that this lens should take an elliptical shape. The long and short axis equal to a and b. The solution for (4.22) can be expressed as

$$l(x_0) = a - a\sqrt{1-\frac{x_0^2}{b^2}} \approx a - a(1-\frac{x_0^2}{b^2}) = \frac{ax_0^2}{2b^2}, \tag{4.25}$$

where the first order Taylor expansion of the square root is applied under the condition that $\frac{x_0}{b}$ is much smaller than 1. Since the lens works as a phaser, the pupil function can be written as

$$P_l = u(x_0,0)Ga(x/D)e^{j\frac{2\pi}{\lambda}\{n_L l(x_0)+n_H[l(\frac{D}{2})-l(x_0)]\}}, \tag{4.26}$$

where $u(x_0,0)$ is the given field at the origin $z=0$. Substituting (4.25) into (4.26) gives

$$P_l = u(x_0,0)Ga(x/D)e^{jkn_H[l(x_0)-\frac{x_0^2}{2f}]}. \tag{4.27}$$

Therefore, according to the Fresnel (near-field) diffraction formula (2.15), the field distribution at the focal line of the lens ($z=f$) is obtained

$$\begin{aligned} u(x,f) &= \sqrt{\frac{n}{j\lambda f}}e^{jkn_H[f+\frac{x^2}{2f}]}\int_{-\infty}^{\infty} e^{jkn_H\frac{x_0^2}{2f}}u(x_0,0)Ga(x/D)e^{jkn_H[l(D/2)-\frac{x_0^2}{2f}]}e^{-jkn_H\frac{xx_0}{f}}dx_0 \\ &= \sqrt{\frac{n}{j\lambda f}}e^{jkn_H[f+\frac{x^2}{2f}+l(D/2)]}\int_{-D/2}^{D/2} u(x_0,0)e^{-jk\frac{xx_0}{n_H f}}dx_0, \end{aligned} \tag{4.28}$$

where $l(0) = l(x_0 = D/2)$. It can be found that the lens plays a role as a spatial Fourier transformer. Physically, the lens corrects spherical wave front to plane wave front by forcing the rays with smaller angle (to the propagation axis) to experience more delays. This correction is only valid with the paraxial assumption under which the spherical wave

is firstly approximated by a parabolic wave. After such correction, the Fresnel transformation becomes the spatial Fourier transformation without the far-field assumption. Also because of such spherical wave to plane wave correction, a point source at the focal line will be collimated by the lens at its aperture.

4.3.2 Lens Design by BPM

According to the mathematical formulation discussed in the previous section, an initial design on the waveguide lens can be obtained. However, in practical case, the input is waveguide mode rather than a point source, and more importantly, the formulation is only valid under the paraxial approximation. As a result, we have to use a more accurate numerical simulation tool to verify and further improve the design. Here, the BPM is employed. The wavelength is chosen as λ_0 =1.55μm. The design data for the lens is shown in Table 4.1

Table 4.1 Structural design of waveguide lens.

Structure parameters	value
Slab effective refractive index n_L	3.2
Mesa effective refractive index n_H	3.6
Input waveguide refractive index n_w	3.25
Input waveguide width (μm)	2
Long axis of the ellipse a (μm)	316
Short axis of the ellipse b (μm)	150.5
Lens focal length f (μm)	628
Lens aperture D (μm)	301

The field distribution after the first lens is depicted in Figure 4.2. To show the collimation properties of the lens, both the amplitude and effective phase after the first

lens along z direction are recorded as shown in Figure 4.3. The effective phase constant is defined as

$$\varphi_{eff} = \frac{-j(\ln F - \ln|F|)}{z_0}, \tag{4.29}$$

where F is the electrical field obtained by BPM.

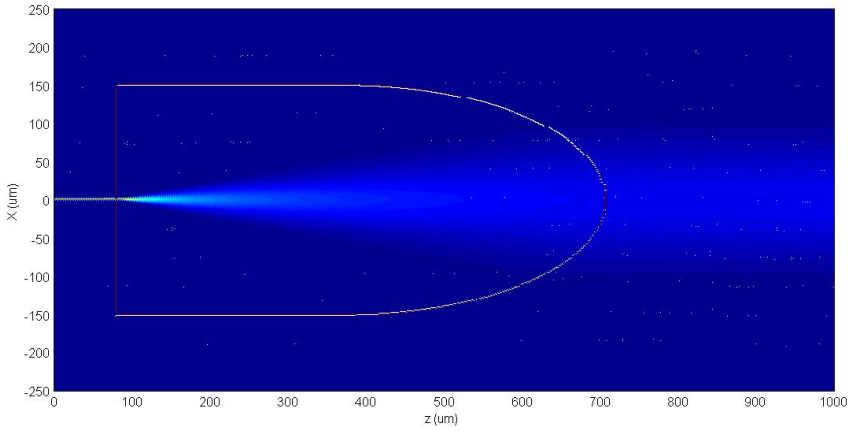

Figure 4.2 Field distribution after the first lens.

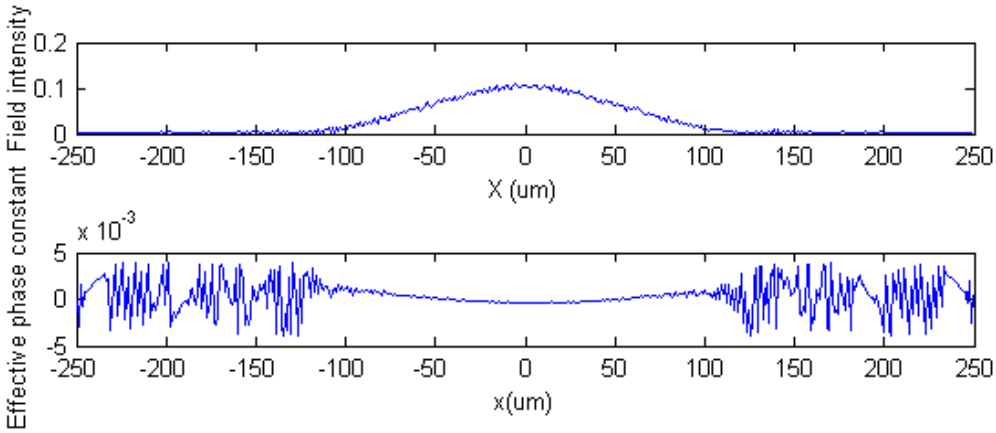

Figure 4.3 Field intensity and effective phase constant after first lens.

It can be seen that input light beam will expand and finally reach planar-like amplitude and phase front as it propagates along z direction.

Consider the structure with two waveguide lenses among which one is collimating and the other is refocusing the light beam from the input waveguide. For simplicity, we selected identical lens design in our example. However, the collimating lens can actually be reduced to allow smaller device size. If the lenses are designed ideally, the light which is collimated by the first lens and then refocused after the second lens should be completely coupled into the output waveguide. Figure 4.4 shows the field distribution for the two lens structure. The insertion loss for the structure is 0.1 dB. For this reason, the waveguide lens can be employed in the TD-OFT system.

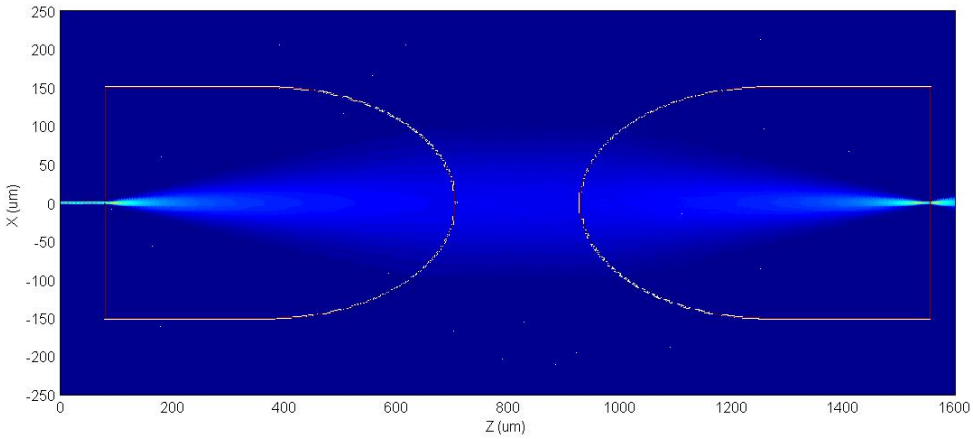

Figure 4.4 Field distribution for the double lens.

4.4 Numerical Verification of TD-OFT

A schematic view is shown in Figure 4.5. It should be noted that the lens are all based on the structure we discussed in the previous section except the third one. Different from the ellipse shape of other lenses, the third lens is a conventional thin lens consisting of two symmetric circle arcs. The parameters of the thin lens and two blazed gratings are presented in Table 4.2.

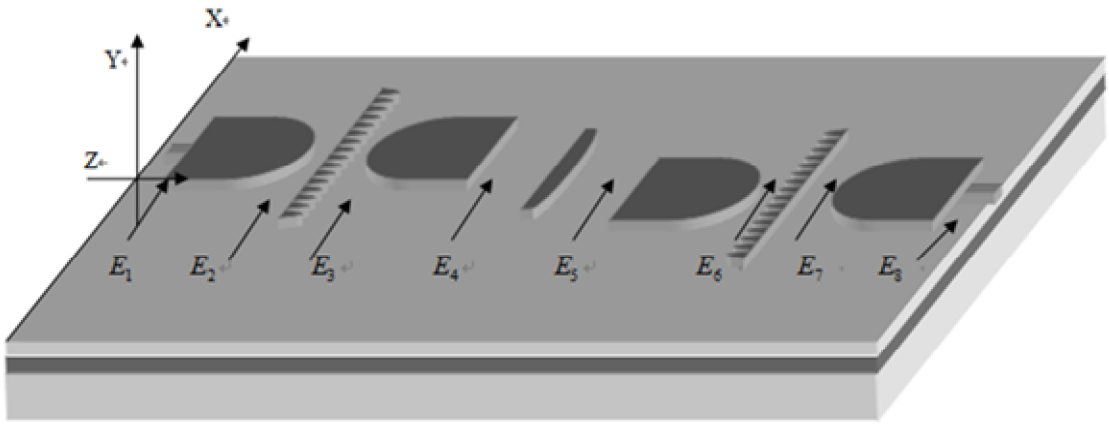

Figure 4.5 Schematic view of the device structure.

Table 4.2 Structural design of thin lens and blazed phase grating.

Structure parameters	value
Slab effective refractive index n_L	3.2
Mesa effective refractive index n_H	3.6
Diffraction grating period T (μm)	7.7
Diffraction grating width d (μm)	3.8
Diffraction order m	-1
The radius of the arcs in thin lens	189.5
Thin lens aperture (μm)	351
Thin lens focal length f_2 (μm)	758

4.4.1 Gaussian Pulse

First, let's consider a Gaussian pulse centered at λ_0 =1.55 μm with pulse duration $\tau = 10$ fs. Given the time to space conversion plays a key role in our design, therefore we will have emphasis on this part in the remainder of this section. Due to the linear optical structure, the pulse can be decomposed into different frequencies. Taking the central frequency for example, the field distribution in the plane of x_4 is plotted in Figure 4.6.

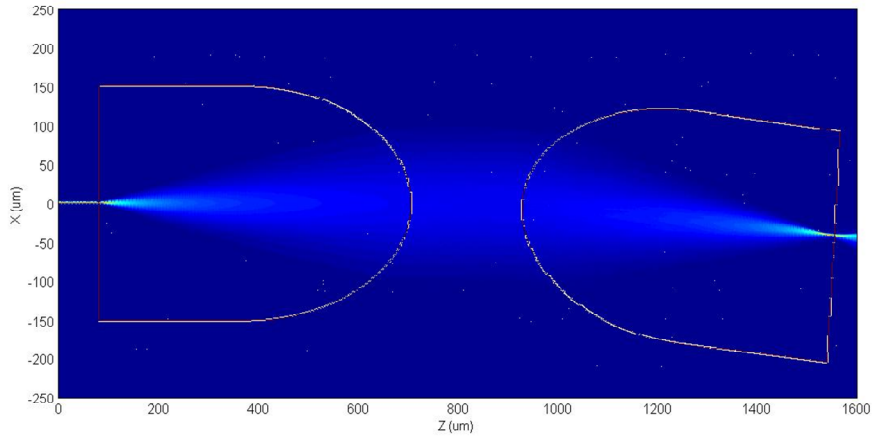

Figure 4.6 Field distribution for the time to space conversion.

It can be seen that the collimated light deflects after passing through the grating and then refocused to a location along x by the second lens. The offset is 42.01μm, which is a little larger than the analytical one 35.12μm ($x_{40} = m\lambda_0 f / n_H T$). It is due to the reason that there is no distance assumed between the grating and the second lens in the mathematical derivation. However, in practical numerical simulations, there exists certain space between these two components. As a result, the offset is enlarged accordingly.

Figure 4.7 shows the field distributions of five wavelength inputs with 0.1μm apart centered at 1.55μm.

As we can see, the longer wavelength provides the larger spatial offset in the focus plane. The values of the peak locations for the five wavelengths are depicted in Table 4.3. It can be found that the separation of 0.1μm is about 2μm which is in good agreement with the analytical results 2.27μm ($\Delta x = m\Delta\lambda_0 f_1 / n_H T$).

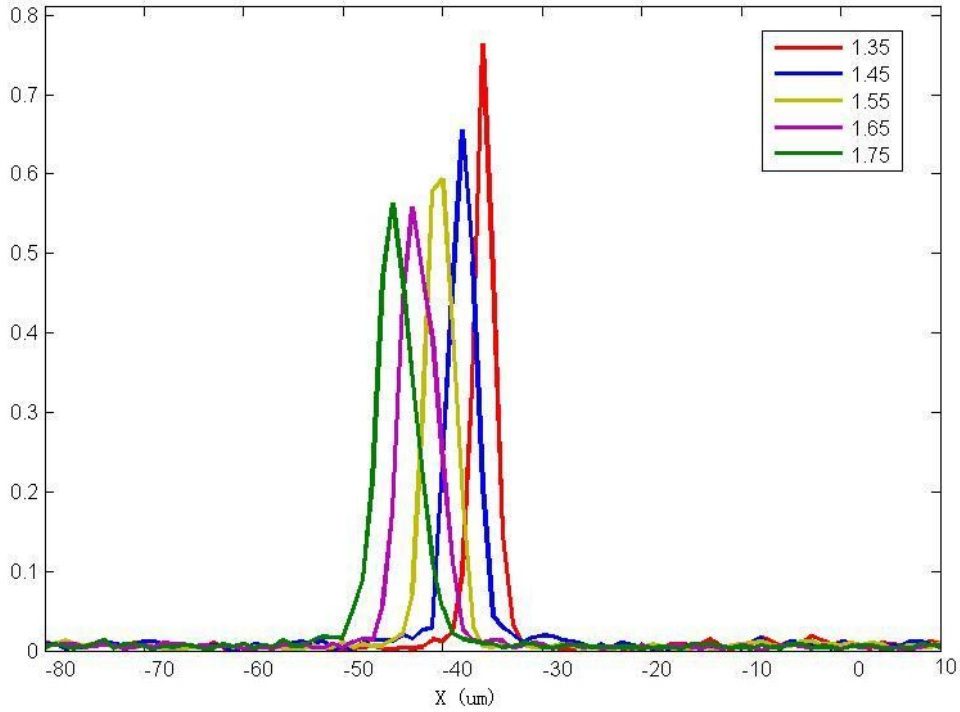

Figure 4.7 Field distributions at the plane of x_4 for the five wavelengths.

Table 4.3 The offsets along x_4 direction for the five wavelengths.

Wavelength(μm)	1.35	1.45	1.55	1.65	1.75
Offset(μm)	-37.8	-40.0	-42.01	-44.01	-46.0

In order to get the entire spatial distribution, different wavelengths are sampled. After the superposition in the frequency domain, the field distribution in the plane of x_4 is obtained. From Figure 4.8, we can see that the spatial distribution corresponds with the scaled spectrum profile.

Following the spatial Fourier transform, the field distribution at the back plane of the third lens is derived as illustrated in Figure 4.9. The spatial distribution nearly shares the same profile with the scaled temporal waveform.

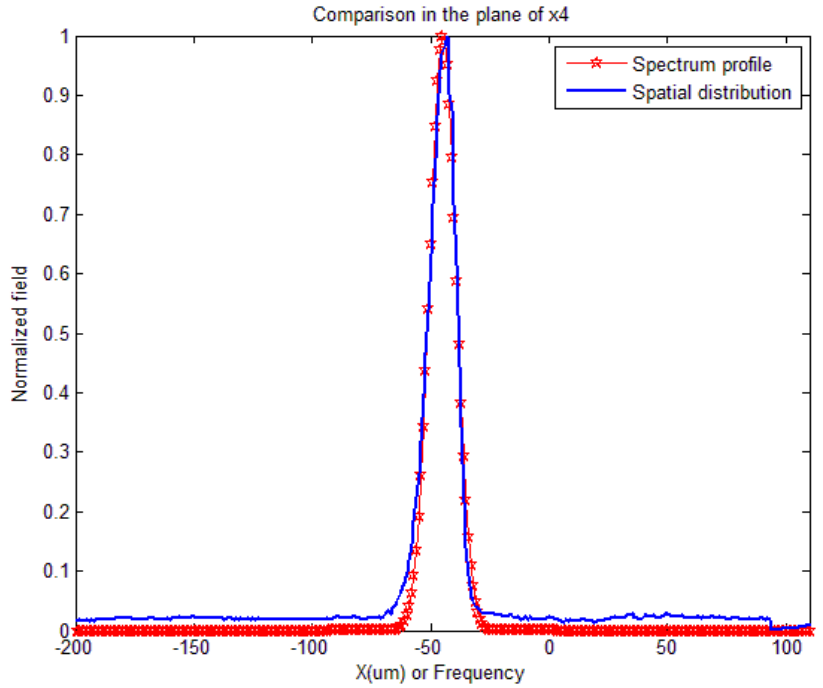

Figure 4.8 Comparison between the spatial distribution and ideal spectrum profile in the plane of x_4 for input Gaussian pulse.

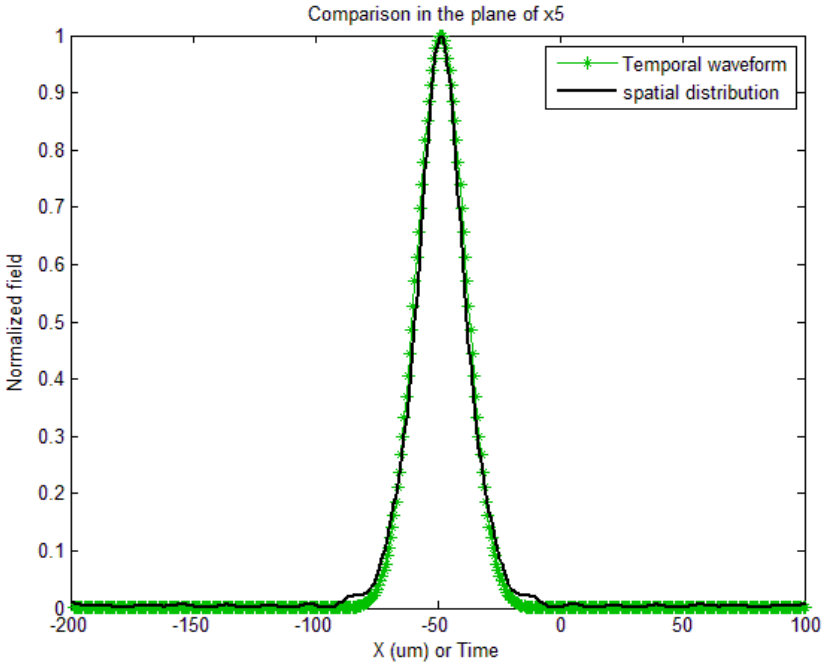

Figure 4.9 Comparison between the spatial distribution and ideal temporal waveform in the plane of x_5 for input Gaussian pulse.

Figure 4.10 shows the output temporal field agrees very well with the analytical waveform, the similarity of these two can be reached to 97.1%. In comparison with the original input pulse, the final output pulse is also compressed in time.

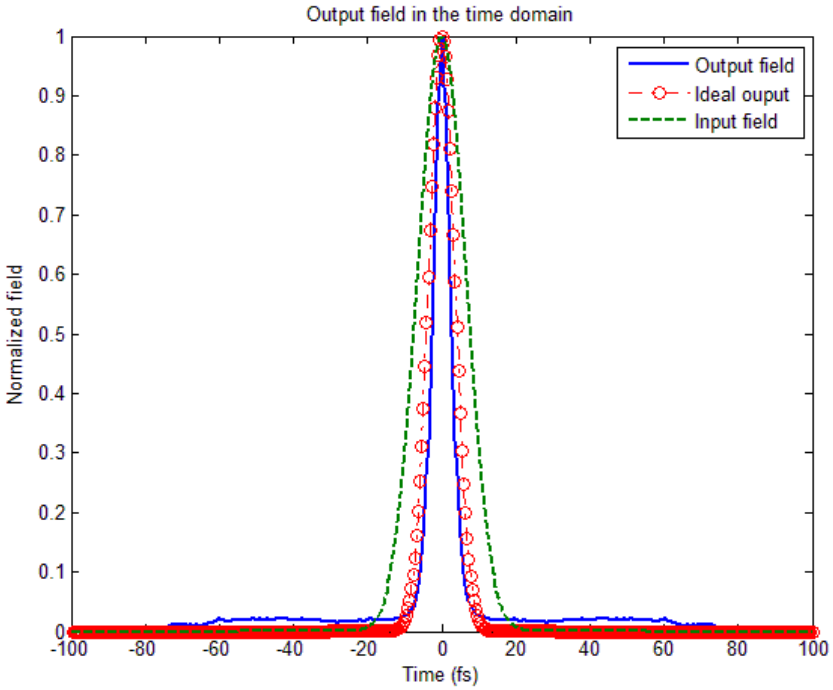

Figure 4.10 Temporal output field for input Gaussian pulse.

According to the reciprocity theorem, the device should also work under the interchange of the source and observer. Therefore, we can use this reciprocity symmetry to verify our design and simulation. For simplicity, let's consider the field amplitude of in the plane of x_5 .The procedures can be illustrated in Figure 4.11.

A) Suppose an input pulse propagates from the left port to the plane of x_4. It is proved that the spatial distribution agrees with the spectrum profile. After passing through the middle thin lens, the waveform of E_5 is obtained. It is a spatial Fourier transform of E_4 and proportional to the temporal waveform. Let's demonstrate it as E_{5l}. B) On the

other hand, the ideal output waveform is launched from right port to the plane of x_5. Similarly, we can get the field distribution which is denoted as E_{5r}. In Figure 4.12, it is shown that E_{5r} is also proportional to its corresponding temporal waveform. C) Then we put the E_{5l} and E_{5r} in the same coordinate, as illustrated in Figure 4.13, they are in a good agreement with each other. Based on the reciprocity in TD-OFT which has been detailed in chapter 3.4, we can safely conclude that both the theoretic analysis and numerical simulation are verified.

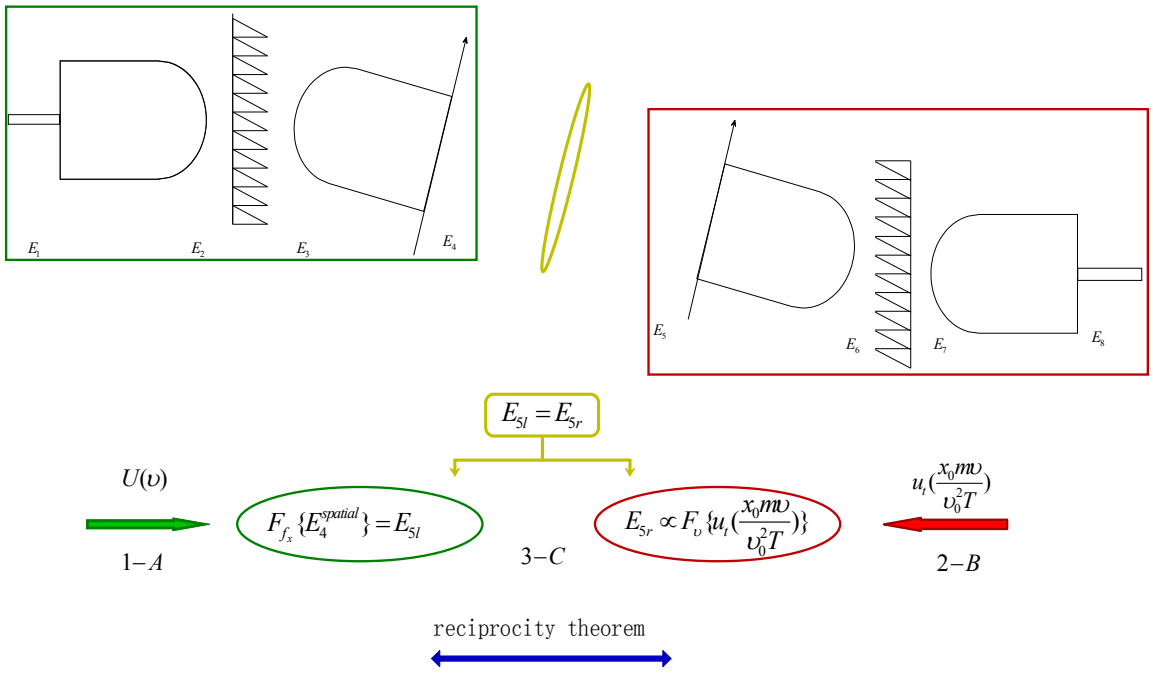

Figure 4.11 Reciprocity in TD-OFT.

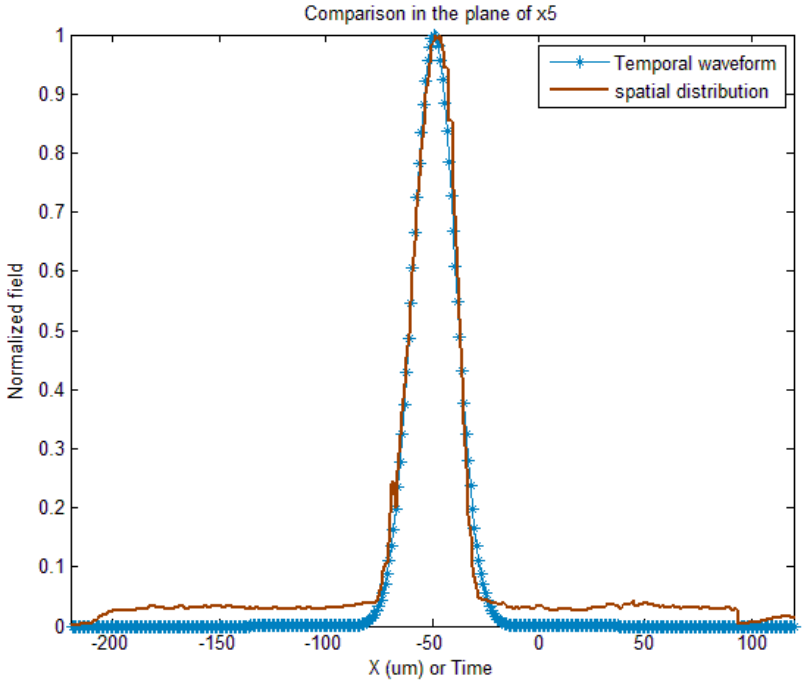

Figure 4.12 Comparison between the spatial distribution E_{5r} and ideal temporal waveform in the plane of x_5 for input Gaussian pulse from the output waveguide.

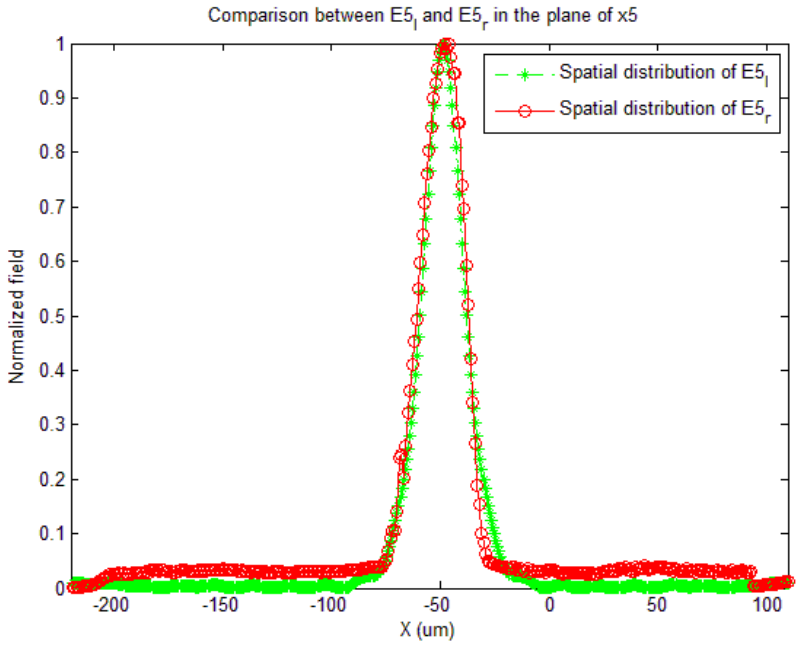

Figure 4.13 Comparison between the spatial distribution of E_{5l} and E_{5r} for the input Gaussian pulse.

4.4.2 Raised Cosine Pulse

Now we examine the Raised cosine pulse with the same structure. The temporal part is denoted as

$$h(t) = \sin c\left(\frac{t}{T_0}\right)\frac{\cos\left(\frac{\pi\beta t}{T_0}\right)}{1-\frac{4\beta^2 t^2}{T_0^2}}, \tag{4.30}$$

with the corresponding spectrum given by

$$H(\upsilon) = \begin{cases} T_0 & |\upsilon| \le \frac{1-\beta}{2T_0} \\ \frac{T_0}{2}\left[1+\cos\left(\frac{\pi T_0}{\beta}\left[|\upsilon|-\frac{1-\beta}{2T_0}\right]\right)\right] & \frac{1-\beta}{2T_0} < |\upsilon| \le \frac{1+\beta}{2T_0} \\ 0 & \text{otherwise} \end{cases} \quad (\beta = 0.95), \tag{4.31}$$

where β is the roll-off factor, here we use $\beta = 0.95$, T_0 =10fs.

Similarly, the spatial distribution in the plane of x_4 agrees with the spectrum profile as shown in Figure 4.14. Moreover, it is also valid when it comes to the field distribution in plane of x_5 and the temporal waveform as shown in Figure 4.15.

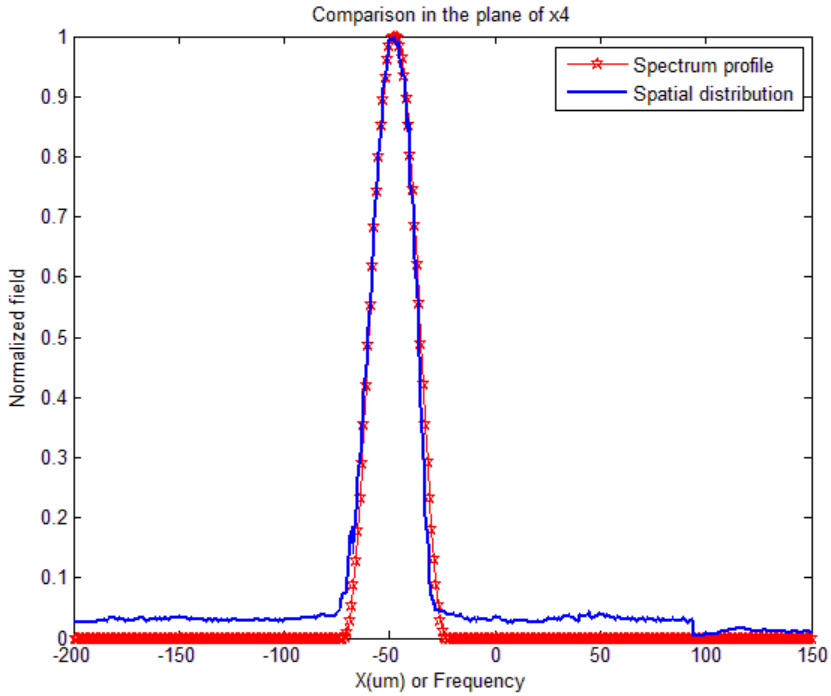

Figure 4.14 Comparison between the spatial distribution and ideal spectrum profile in the plane of x_4 for raised cosine pulse.

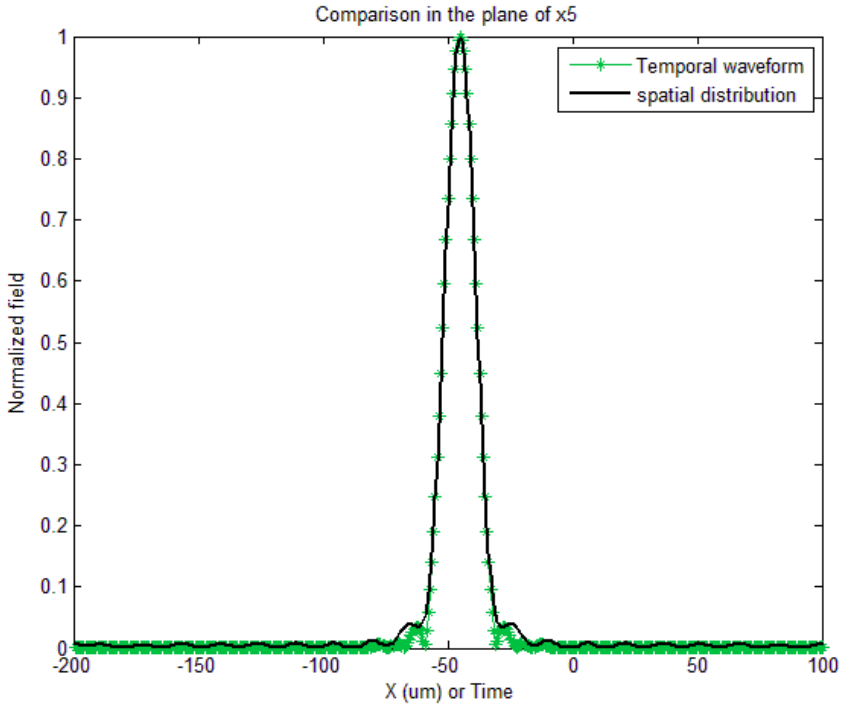

Figure 4.15 Comparison between the spatial distribution and ideal temporal waveform in the plane of x_5 for input raised cosine pulse.

From Figure 4.16, it is clearly found that the real output temporal field is in a good agreement with our analytical result, the similarity is calculated as 98.7% . In other words, it is proportional to the Fourier transform of the input temporal pulse. Also, we can see the output filed is stretched in time compared with the original input pulse.

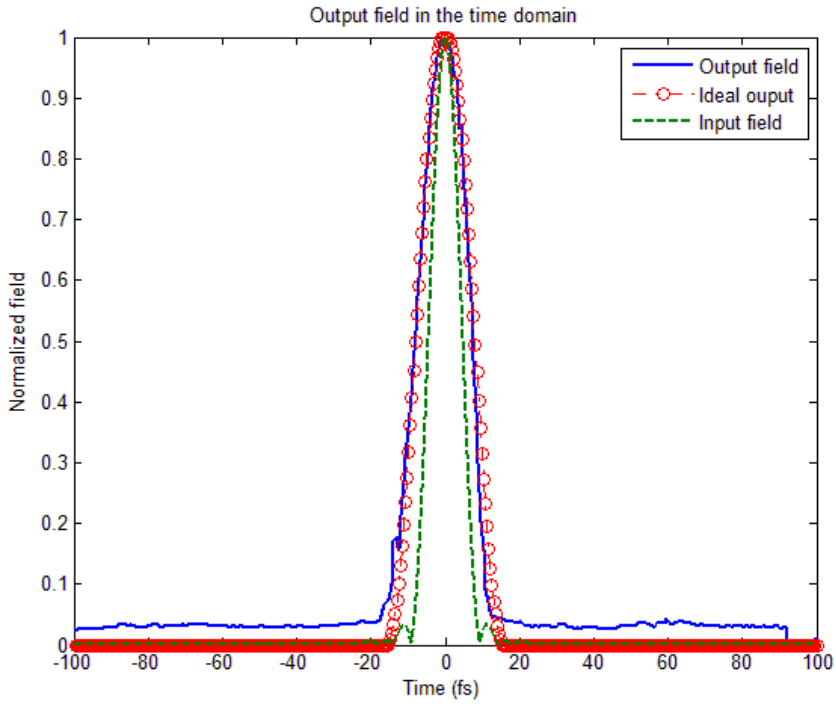

Figure 4.16 Temporal output field for input raised cosine pulse.

To further verify our results, again, reciprocity theorem is employed. If we illuminate the device from the right hand side with theoretic output field, then in the plane of x_5, the spatial distribution E_{5r} is given by Figure 4.17. For the sake of comparison, it is presented together with E_{5l} which denotes the field amplitude obtained from original input pulse at the left hand side. In Figure 4.18, we can find that E_{5r} is in a good agreement with E_{5l}. Therefore, with the help of the reciprocity in TD-OFT, the design concept and the simulation results are verified.

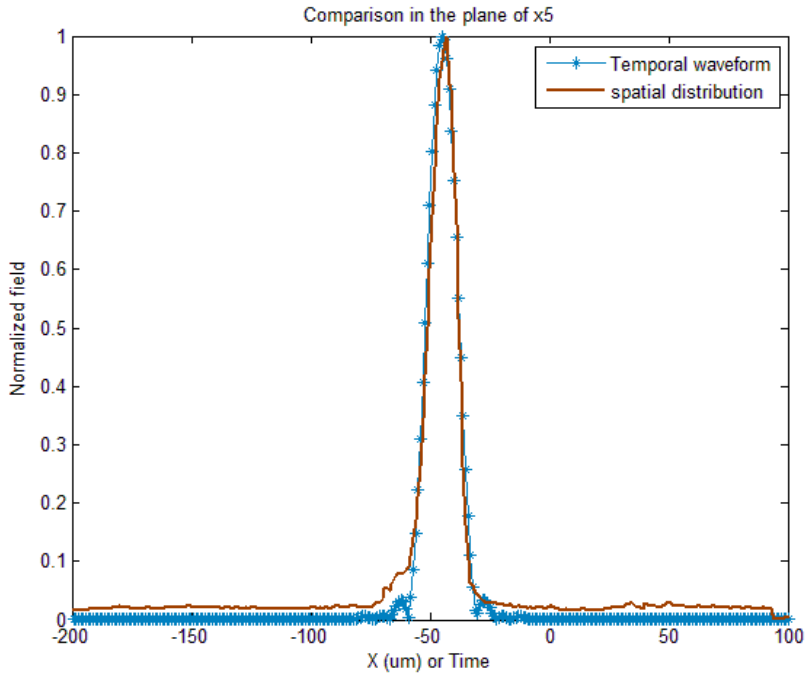

Figure 4.17 Comparison between the spatial distribution E_{5r} and ideal temporal waveform in the plane of x_5 for input raised cosine pulse from the output waveguide.

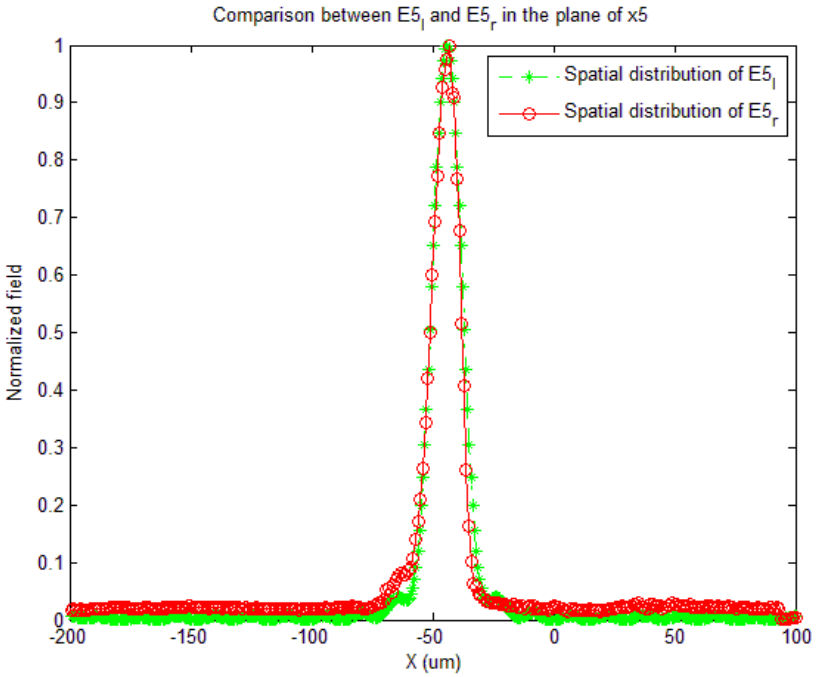

Figure 4.18 Comparison between the spatial distribution of E_{5l} and E_{5r} for the input raised cosine pulse.

4.5 Summary

In this chapter, we have numerically simulated the novel design for planar integrated TD-OFT by combining carefully designed waveguide lenses and blazed phase gratings. Two input examples have been chosen to study the device performance and the similarity can be achieved 97.1% ，98.7% respectively with the structure. In addition, the reciprocity theorem is also applied to verify both the theoretic results and numerical simulation. The design presented in this chapter has shown that the new planar waveguide TD-OFT has the potential of reducing the device size and fabrication cost.

Chapter 5
Conclusion and Future Work

5.1 Conclusion

The objective of this thesis is to design, modeling and simulate a novel planar waveguide TD-OFT. This device occupies a size about $600\mu m$ (in width) $\times$ 5mm (in length) for an ultrafast pulse around $10\,fs$. We find the similarity between the output temporal profile and the Fourier transform profile of the original pulse can be achieved above 97%. It is possible to make the device size even smaller either by reducing the focal length of the collimating lens or enlarging the bandwidth of input pulse.

Compared with currently proposed TD-OFT made by discrete photonic and optoelectronic components, this design can be integrated with a more compact size and potentially reduce the cost. As a result, the planar waveguide TD-OFT has great potential in the next ultrafast optical network.

5.2 Suggestions for Future Work

Although the advantages of our designed TD-OFT have been demonstrated, there still remain some topics worth further studying.

1. Space-time coupling. In the previous theoretical treatment, for the initial input pulse, it is assumed that the space and time field components can be separated. However,

this assumption is not accurate enough to be used in femtosecond region. It is due to the fact that the couplings among the beam parameters in space and time will emerge on propagation of the pulse [39-41]. Accordingly, the effects of the coupling between the spatial and temporal properties of the pulse upon the propagation need to be further investigated.

2. Time- domain BPM. In this thesis, the extension BPM is applied to simulate the device. However, it is still based on the conventional BPM in frequency domain and therefore not directly applicable for simulation of the ultrafast pulse propagation in time domain. Moreover, neither three-dimensional effects nor the edge reflections are considered in the simulation. To overcome the limitations, a more straightforward and accurate time-domain BPM for modeling the optical waveguide devices is demanded in future work.

Bibliography

[1] M. Tokurakawa, *et al.*, "Ultrashort pulse generation from diode pumped mode-locked Yb3+:sesquioxide single crystal lasers," *Opt. Express,* vol. 19, pp. 2904-2909, 2011.

[2] C. Bourassin-Bouchet, *et al.*, "Control of the attosecond synchronization of XUV radiation with phase-optimized mirrors," *Opt. Express,* vol. 19, pp. 3809-3817, 2011.

[3] B. Jalali, *et al.*, "Silicon photonics: Silicon's time lens," *Nat Photon,* vol. 3, pp. 8-10, 2009.

[4] J. Giordmaine, *et al.*, "Compression of optical pulses," *Quantum Electronics, IEEE Journal of,* vol. 4, pp. 252-255, 1968.

[5] A. M. Weiner, "Ultrafast optical pulse shaping: A tutorial review," *Optics Communications,* vol. 284, pp. 3669-3692, 2011.

[6] D. R. Solli, *et al.*, "Amplified wavelength-time transformation for real-time spectroscopy," *Nat Photon,* vol. 2, pp. 48-51, 2008.

[7] M. M. Wefers and K. A. Nelson, "Analysis of programmable ultrashort waveform generation using liquid-crystal spatial light modulators," *J. Opt. Soc. Am. B,* vol. 12, pp. 1343-1362, 1995.

[8] Y. Dong and S. Kumar, "Realization of optical OFDM using time lenses and its comparison with conventional OFDM for fiber-optic Systems," in *Optical*

Communication, 2009. ECOC '09. 35th European Conference on, 2009, pp. 1-2.

[9] T. Jannson, "Real-time Fourier transformation in dispersive optical fibers," *Opt. Lett.,* vol. 8, pp. 232-234, 1983.

[10] A. W. Lohmann and D. Mendlovic, "Temporal filtering with time lenses," *Appl. Opt.,* vol. 31, pp. 6212-6219, 1992.

[11] B. H. Kolner, "Space-time duality and the theory of temporal imaging," *Quantum Electronics, IEEE Journal of,* vol. 30, pp. 1951-1963, 1994.

[12] D. Grischkowsky and A. C. Balant, "Optical pulse compression based on enhanced frequency chirping," *Applied Physics Letters,* vol. 41, pp. 1-3, 1982.

[13] L. K. Mouradian*, et al.*, "Spectro-temporal imaging of femtosecond events," *Quantum Electronics, IEEE Journal of,* vol. 36, pp. 795-801, 2000.

[14] B. H. Kolner and M. Nazarathy, "Temporal imaging with a time lens," *Opt. Lett.,* vol. 14, pp. 630-632, 1989.

[15] B. H. Kolner, "Active pulse compression using an integrated electro-optic phase modulator," *Applied Physics Letters,* vol. 52, pp. 1122-1124, 1988.

[16] C. V. Bennett and B. H. Kolner, "Principles of parametric temporal imaging. I. System configurations," *Quantum Electronics, IEEE Journal of,* vol. 36, pp. 430-437, 2000.

[17] M. A. Muriel*, et al.*, "Real-time Fourier transformer based on fiber gratings," *Opt. Lett.,* vol. 24, pp. 1-3, 1999.

[18] R. Salem*, et al.*, "Optical time lens based on four-wave mixing on a silicon chip," *Opt. Lett.,* vol. 33, pp. 1047-1049, 2008.

[19] M. A. Foster*, et al.*, "Ultrafast waveform compression using a time-domain telescope," *Nat Photon,* vol. 3, pp. 581-585, 2009.

[20] I. P. Kaminow, "Optical Integrated Circuits: A Personal Perspective," *Lightwave Technology, Journal of,* vol. 26, pp. 994-1004, 2008.

[21] J. W.Goodman, *Introduction to Fourier Optics*, 2nd ed. New York: McGraw-Hill Science, 1996.

[22] G. Zhou, "Design, modeling and simulation of planar waveguide demultiplexers," Ph.D., McMaster University, Canada, 2007.

[23] E. W. Max Born, *Principles of optics*, 7 ed. Cambridge: Cambridge University Press, 1999.

[24] M. Gruber, "Multichip Module with Planar-Integrated Free-Space Optical Vector-Matrix-Type Interconnects," *Appl. Opt.,* vol. 43, pp. 463-470, 2004.

[25] G.-R. Z. Xun Li, Ning-Ning Feng, Weiping Huang, "A novel planar waveguide wavelength demultiplexer design for integrated optical triplexer transceiver," *Photonics Technology Letters,* vol. 17, pp. 1214-1216, June 2005.

[26] D. F. Williams and R. B. Marks, "Reciprocity relations in waveguide junctions," *Microwave Theory and Techniques, IEEE Transactions on,* vol. 41, pp. 1105-1110, 1993.

[27] G. Shu and T. T. Charalampopoulos, "Reciprocity Theorem for the Calculation of Average Scattering Properties of Agglomerated Particles," *Appl. Opt.,* vol. 39, pp. 5827-5833, 2000.

[28] D. Pissoort and F. Olyslager, "Study of eigenmodes in periodic waveguides using

the Lorentz reciprocity theorem," *Microwave Theory and Techniques, IEEE Transactions on,* vol. 52, pp. 542-553, 2004.

[29] C. Shun-Lien, "A coupled mode formulation by reciprocity and a variational principle," *Lightwave Technology, Journal of,* vol. 5, pp. 5-15, 1987.

[30] Y. Chung and N. Dagli, "An assessment of finite difference beam propagation method," *Quantum Electronics, IEEE Journal of,* vol. 26, pp. 1335-1339, 1990.

[31] F. Wijnands*, et al.*, "Modal fields calculation using the finite difference beam propagation method," *Lightwave Technology, Journal of,* vol. 12, pp. 2066-2072, 1994.

[32] W. P. Huang*, et al.*, "The perfectly matched layer (PML) boundary condition for the beam propagation method," *Photonics Technology Letters, IEEE,* vol. 8, pp. 649-651, 1996.

[33] G. R. Hadley, "Wide-angle beam propagation using Padé approximant operators," *Opt. Lett.,* vol. 17, pp. 1426-1428, 1992.

[34] G. R. Hadley, "Multistep method for wide-angle beam propagation," *Opt. Lett.,* vol. 17, pp. 1743-1745, 1992.

[35] F. Ning-Ning and H. Wei-Ping, "Time-domain reflective beam propagation method," *Quantum Electronics, IEEE Journal of,* vol. 40, pp. 778-783, 2004.

[36] H. M. Masoudi, "A Stable Time-Domain Beam Propagation Method for Modeling Ultrashort Optical Pulses," *Photonics Technology Letters, IEEE,* vol. 19, pp. 786-788, 2007.

[37] M. Koshiba*, et al.*, "Time-domain beam propagation method and its application to

photonic crystal circuits," *Lightwave Technology, Journal of,* vol. 18, pp. 102-110, 2000.

[38] L. Gomelsky and J. M. Liu, "Extension of beam propagation method to time-dependent optical waveforms," *Photonics Technology Letters, IEEE,* vol. 6, pp. 546-548, 1994.

[39] W. Zhongyang, *et al.*, "Space-time profiles of an ultrashort pulsed Gaussian beam," *Quantum Electronics, IEEE Journal of,* vol. 33, pp. 566-573, 1997.

[40] F. Frei, *et al.*, "Space-time coupling in femtosecond pulse shaping and its effects on coherent control," *Journal of Chemical Physics,* vol. 130, p. 034302, 2009.

[41] B. J. Sussman, *et al.*, "Focusing of light following a 4-f pulse shaper: Considerations for quantum control," *Physical Review A,* vol. 77, p. 043416, 2008.